

1 **Analogous biomineralization processes between the fossil coral *Calceola***
2 ***sandalina* (Rugosa, Devonian) and other Recent and fossil cnidarians.**

3 Ismael Coronado,^{1,*} Alberto Pérez-Huerta,² Sergio Rodríguez^{1,3}

4 ¹ *Departamento de Paleontología, Universidad Complutense de Madrid. C/ José Antonio*
5 *Nováis 2, Ciudad Universitaria. E-28040 Madrid. Spain. ismael.coronado@geo.ucm.es*

6 ² *Department of Geological Sciences, University of Alabama, Tuscaloosa AL 35487, USA.*
7 *aphuerta@as.ua.edu*

8 ³ *Instituto de Geociencias (IGEO. CSIC-UCM). C/ José Antonio Nováis 2, Ciudad*
9 *Universitaria. E-28040 Madrid. Spain. sergrodr@geo.ucm.es*

10 * *Corresponding author*

11 **Abstract**

12 The current work represents a distinctive study about the biomineral properties of
13 exceptionally good preserved skeletons of *Calceola sandalina* from the Middle Devonian of
14 Couvin (Belgium), Smara (Morocco) and (Algeria) and their relation in the evolution of
15 biomineralization of cnidarians. . Structural and crystallographic analyses of the skeletons have
16 been done by petrographic microscopy, electron scanning microscopy (SEM), atomic force
17 microscopy (AFM), electron backscatter diffraction (EBSD), computer-integrated polarization
18 microscopy (CIP) and electron microprobe analysis (EMPA). *Calceola* skeletons have many
19 similarities with other cnidarians, mainly with other Palaeozoic corals as Syringoporicae: The
20 microcrystals are composed of co-oriented nanocrystals that remind to mesocrystals, suggesting
21 a biocrystallization process by particle attachment (CPA). The relationship between the
22 nanocrystals and microcrystals suggest a growth mode similar to mineral bridges. A similar
23 model was described for Syringoporicae corals (Tabulata) and it is similar to the coordinated-
24 growth mode described in scleractinians and molluscs. *Calceola* skeletons show also a
25 convergent structure with scleractinian forming Rapid Accretion Deposits (RAD), which share

26 some structural and chemical properties. These evidences suggest analogous processes of
27 biomineralization derived from a stem group of cnidarians. The results of this paper highlight
28 the value of biomineralization studies in fossil organisms to understand the evolution of
29 biomineralization mechanism through Phanerozoic.

30 Keywords: calcite, Rapid Accretion Deposits, stepped coordinated-growth mode, mineral
31 bridges, evolution, biocrystallization.

32 **Introduction**

33

34 The phylum Cnidaria appears to have one of the longest fossil histories (2000 m.y.) and
35 uncertain among the metazoan phyla (Scrutton, 1979), probably due to their morphological
36 simplicity and gaps in the fossil record, which does difficult to recognise lineages. In fact, the
37 mineralised record of cnidarian, although have a better understanding, is charged of controversy
38 due to this lacks in the record (cites herein Coronado *et al.*, 2013). During the Cambrian
39 radiation, Tommotian onwards, appeared sporadically new organisms with mineralized
40 skeletons that could be the ancestors of Palaeozoic Anthozoa (*e.g.* Hydroconozoa and
41 Tabulacnoids (Porter, 2010), uncertain Tabulata (Lafuste, 1991) and cothonids (Korde, 1959),
42 among others). Nevertheless it was not until early Ordovician when the Palaeozoic corals
43 appeared (Tabulata and later Rugosa), which radiating very quickly, occupying empty
44 ecological niches and colonizing most environments in the Palaeozoic seas during more than
45 233 Ma.

46 After the Permian extinction, when Palaeozoic corals disappeared, the scleractinian
47 dominated the seas during 247 Ma, but during 5 m.y. in early Triassic there is not record of
48 mineralized cnidarian. However, the knowledge about their evolution, in terms of
49 biomineralization pathways, is unresolved because the evolutionary link between Palaeozoic
50 corals and scleractinian is actually controversial (Oliver, 1980, Sorauf, 1996, Ezaki, 1998, Cuif,
51 2014). Molecular studies in anemones and corals suggest an origin of Scleractinia rooted in the

52 Palaeozoic (at least 300 Ma. Romano & Palumbi, 1966; Medina *et al.*, 2006; around 425 Ma.
53 Stolarski *et al.*, 2011). On the other hand, Cuif *et al.* (2011) and Cuif (2014) have compared the
54 biocrystallization processes between Permian and Triassic corals with the purpose to solve the
55 evolutionary lineage between Rugosa and Scleractinia, as was suggested by Wang (1950),
56 establishing common morphological and biocrystallization processes between Polycoelidae
57 (Rugosa, Permian) and Pachitecalids (Scleractinian, Middle Triassic), although with marked
58 differences.

59 The phylum Cnidaria is represented in the geological record mainly by the corals. This
60 informal grouping refers to the skeletonized members of the Anthozoa class (Tabulata, Rugosa,
61 Scleractinia and Octocorallia, among others). Three mineral groups have been detected in
62 cnidarian (phosphates, sulphates and carbonates), being the carbonates the most abundant both
63 in fossil and Recent organisms (Lowenstan and Weiner, 1989; Macintyre *et al.*, 2000).
64 Carbonates are ubiquitous in Anthozoa class (Cambrian to Recent), in form of spicules and
65 skeletons of Mg-calcite and aragonite in a genera (Octocorallia) and as skeletons of calcite and
66 aragonite (Rugosa, Tabulata, Heterocorallia and Scleractinia), known as stony corals, but also in
67 Hydrozoa skeletons such as Milleporidae and Stylasteridae (Rahman *et al.*, 2006; Cuif *et al.*,
68 2011; Coronado *et al.*, 2013; Janiszewska *et al.*, 2011).

69 The most common biomineralization studies on cnidarian have been focused mainly in
70 fossil and modern Scleractinian (Cuif *et al.*, 2011; Stolarski, 2003; Stolarski and Mazur, 2005,
71 Tambutté *et al.*, 2011; Janiszewska *et al.*, 2011, 2015) and recent octocorals (Dauphin *et al.*,
72 2006; Vielzeuf, 2010, Rahman and Yeishin. 2005; Rahman *et al.*, 2006). Classically, the
73 microstructural studies in Palaeozoic corals have been driven to identify and classify
74 evolutionary patterns of biocalcification and their applications as taxonomical criteria (Wang,
75 1950; Wang & Chen, 1989; Lafuste, 1981; Lafuste & Plusquellec, 1985).

76 Biominerals (*sensu* Marin *et al.*, 2014) offer chemical information about the original
77 environmental conditions (by geochemical proxies). They also offer a possibility to understand
78 the growth processes that provide to organisms an evolutionary advantage to colonize different
79 habitats (e.g., growth patterns Barbin *et al.*, 2008; changes in mineralogy Benedix *et al.*, 2014;

80 formation of structural elements Pérez-Huerta, *et al.*, 2009, etc). The importance of
81 biomineralization studies in fossils can help to understand the evolution of metazoan through
82 Phanerozoic. Numerous articles have developed biomineral studies in different fossils; molluscs
83 (Mutvei, 1997; Dauphin, 2002; Vendrasco, 2013), brachiopods (Williams and Wright, 1970;
84 Balthasar *et al.*, 2011), cnidarians (Sorauf, 1980; Stolarski 2003; Stolarski and Mazur, 2005
85 Coronado *et al.*, 2013), porifera (Retiner and Engeser, 1987; Cuif *et al.* 2011) and trilobites
86 (McAllister and Brand, 1989; Dalingwater, 1973; Lee *et al.* 2012) among others. Comparative
87 studies of fossil and recent organisms considering their processes of biocrystallization,
88 strategies and features, can also solve paleontological problems such as uncertain systematic
89 affinities (Coronado *et al.*, 2015c). Likewise, these studies can help to understand the
90 biomineralization in evolutionary terms, as common strategies of biocrystallization (Towe,
91 1978; Cuif et l., 2011), structures and chemical properties driven for the global geochemistry
92 (Sandberg, 1983; Checa *et al.*, 2007a;Stolarski et al., 2007)).

93 The crystallo-chemical properties (*sensu* Mann, 2001; Coronado *et al.*, 2013) of
94 biominerals that compose the fossil skeletons are not easily determined because they often are
95 obliterated by diagenetical processes. Following this line, new advances on biomineralization of
96 Palaeozoic corals have been focused on the biogenic origin of skeletons of Carboniferous
97 Syringoporicae (Coronado *et al.* 2013; Coronado *et al.* 2015a, 2015b; Coronado and Rodríguez,
98 2015) a superfamily of tabulate corals, taking special interest in the diagenetical alteration,
99 establishing of a biocrystallization model for this group. It is remarkable these studies are only
100 the starting place to advance in the evolution of cnidarians from biomineralization.

101 The current work represents an innovative study about the biomineral (crystallo-chemical)
102 properties preserved in the skeletons of an unusual rugose coral (*Calceola sandalina*) and their
103 relation in the evolution of biomineralization of Palaeozoic corals regarding the aforementioned
104 work.

105 The slipper coral *Calceola sandalina* is a common coral in Devonian rocks (Termier &
106 Termier, 1948; Lafuste, 1983; Hill & Jell, 1969; Stolarski, 1993; Gudo, 1998; Galle & Ficner,
107 2004). This taxon belongs to Goniophyllidae, a family of operculate Palaeozoic corals with a

108 distribution from Cambrian? to Devonian (Stolarski, 1993). The unusual morphology of
109 *Calceola* and their operculum turned this taxon into a controversial topic for palaeontologists
110 during more than a century, including it in different phyla (Kunth, 1986; Linstroem, 1882;
111 Kowalski, 1983; Richter, 1929). *Calceola sandalina* is an ahermatipic coral that inhabited soft-
112 bottom substrates and is typically found in moderate- to deep-water sediments (Jakubowicz *et*
113 *al.*, 2015). Lafuste (1983) compared the microstructure of *Calceola* (one sample of this study)
114 and *Goniophyllum* (from Silurian of Sweden), concluding that both microstructures are similar
115 with slight differences. *Goniophyllum* show a cupolar microlamellar structure similar to other
116 rugose corals, whereas *Calceola* has ‘scutellate’ and plier-shaped microlamellae. This author
117 suggested that although *Calceola* looks very close to *Goniophyllum*, could be considered as a
118 genus *incertae sedis*.

119

120 **Material and Methods**

121

122 Five skeletons of *Calceola* were selected in the Lafuste’s Collection from the Muséum
123 National d’Histoire Naturelle (MNHN) of Paris (France). One sample come from the Middle
124 Devonian (Eifelian, 393.3-387.7 Ma) of Couvin (Belgium), label A47628, were collected by
125 Ms. D. Jacob (Lafuste, 1983); two samples from Smara (Morocco, old Spanish Sahara); Middle
126 Devonian (Givetian, 387.7-382.7 Ma), label A47629 - A47630, were collected by a unknown
127 collector and the two samples from Gara Djebilet (Algerian Sahara), Middle Devonian
128 (Givetian, 387.7-382.7 Ma), label A47631 - A47632, were collected by Sr. P. Semenoff-Tian-
129 Chansky (data of locality in Lafuste and Semenoff-Tian-Chansky, 1968). The taxonomic
130 identification was done by Dr J. Lafuste and Dr. P. Semenoff-Tian-Chansky. Samples from
131 various geological sites have been used to try to minimize artefacts due to the fossilization
132 processes (diagenesis).

133

134 A multilevel study to recognize the structure, crystallographic arrangement and
135 geochemistry by means of different techniques was achieved. The microstructure was studied

136 by petrographic microscopy (in all samples), electron scanning microscopy (SEM) (only at the
137 Belgian sample, A47628), at microscale, and atomic force microscopy (AFM), at nanoscale,
138 (only at the Belgian sample, A47628). The crystallographic properties and arrangement was
139 studied by Computer-Integrated Polarization microscopy (CIP) at mesoscale (in all samples)
140 and Electron Backscatter diffraction (EBSD) at microscale (at the Belgian sample, A47628 and
141 Algerian samples, A47629-A47630). Besides the geochemical characterization was done using
142 an electron microprobe analysis (EMPA) (at the Belgian sample, A47628). Microstructural and
143 crystallographic analyses have not revealed differences between the different samples,
144 reinforcing the study from a biomineral approximation.

145

146 ***Structural characterization***

147 Ultra-thin sections from longitudinal and transverse sections were prepared using the
148 method developed by Lafuste (1970); for correct visualization of microcrystals under
149 petrographic microscopy the samples should be between 2 and 10 μm in thickness. The samples
150 were uncovered and the surfaces were polished with alumina of 1 and 0.05 μm in the final
151 process.

152 In addition, sample fragments, obtained by means of natural breakage of the skeleton, were
153 prepared in order to observe the crystalline elements in three dimensions. SEM images were
154 obtained with a scanning electron microscope JEOL JSM-6400 operated to 20 kV, equipped
155 with an EDX system, located in the National Centre of Electron Microscopy (Universidad
156 Complutense of Madrid, Spain). The samples were coated with a thin conducting carbon and
157 gold coating and observed using secondary electrons.

158 The skeleton counterpart of thin sections, that presented better preservation, were selected
159 to study with AFM. The samples were polished (polished with alumina of 1 μm , 0.3 μm , 0.05
160 μm) and cut forming thin slides and etched with a Milli-Q water solution for 7 h and observed
161 with an Atomic Force Microscope, model Digital Instruments Nanoscope IIIA (Veeco), located
162 at the National Centre of Electron Microscopy, Universidad Complutense de Madrid, Spain.
163 The images were obtained at room temperature and in air using a tapping mode with a silica tip.

164 The images were processed with the Nanoscope software v5.30 r3 sr3 of Veeco Instruments Inc.
165 and the WSxM v5.0 Develop 5.0 software of Nanotec (Horcas *et al.* 2007).

166 ***Crystallographic characterization***

167 Slides were prepared by sectioning of transversal and longitudinal sections of *Calceola*.
168 The slides were polished with alumina of 1 μm , 0.3 μm , 0.05 μm and finally polished with
169 colloidal silica (0.06 μm) for EBSD analysis. Before analysis, samples were coated with a thin
170 layer (1.5 nm) of Au/Pt (Pérez-Huerta and Cusack, 2009). The EBSD study has been carried out
171 with an Oxford Nordlys camera mounted on a Field Emission Scanning Electron Microscope
172 (FE-SEM) JEOL 7000 located in the Central Analytical Facility (CAF) of The University of
173 Alabama. EBSD data were collected with Oxford Aztec 2.0 software at high vacuum, 30 kV,
174 large probe current, and a resolution of 0.3 μm step size for crystallographic maps, and a
175 working distance of about 10 mm. Finally, data were analysed using OIM 5.3 from EDAX-TSL.
176 In this study, EBSD data are represented by crystallographic maps and pole figures, which
177 represent the stereographic projection of crystallographic planes in reference to the {0001}
178 calcite plane. MATLABTM toolbox MTEX (Bachmann *et al.* 2011) was used to plot the ODF
179 (orientation density functions) of the EBSD maps. The GrainsSet is a tool of MTEX that has
180 been chosen to determine grains differentiation, the analysis of misorientation and the
181 representation of the pole figures in the plane {10 $\bar{1}$ 4}, which better represent the turbostratic
182 distribution of crystals (Checa *et al.*, 2007b; Coronado *et al.*, 2015a), in the case there.

183 Ultra-thin sections (transverse and longitudinal) of all specimens were used for CIP
184 (computer-integrated-polarization microscopy), independently of the preparation method of
185 ultra-thin sections (cover or uncovered), using a petrographic Zeiss microscope with a reflex
186 camera attached and a Kodak Wratten filter no. 25. The analysis have been performed at 10x
187 magnifications (resolution of 3072 x 2048 pixel and the ratio pixel- μm is 1:1.14) to determine
188 the crystallographic arrangement of coral skeleton microstructure at mesoscale. The CIP method
189 (computer-integrated-polarization microscopy) has been described by Heilbronner & Barret
190 (2014) as a method for texture analysis and optical orientation imaging. It determines the *c*-axis
191 orientations of uniaxial minerals from optical micrographs, displaying the results in the form of

192 pole figures and orientation images, using a colour-code (CLUT), which represents each
193 orientation. This method has been applied to biomineralization studies of fossil specimens with
194 relevant results (Coronado *et al.*, 2015b,c and Coronado and Rodríguez, 2015). The CIP
195 analyses have been done with Image SXM software (Barret, 1997).

196 ***Geochemical characterization***

197 Electron microprobe analysis was conducted on polished slides with a carbon coating, with
198 a JEOL Superprobe JZA-8900 with five wavelength-dispersive spectrometers, located at the
199 National Centre of Electron Microscopy (the Universidad Complutense of Madrid, Spain).

200 A quantification of some major, minor and trace elements (MTE) was made with EMPA in
201 coral skeleton in random points (100 points). Nine elements were analysed (Ca, Mg, Sr, S, Ba,
202 Na, Mn, Fe and P) at each point and two transverse sections were made sectioning Rapid
203 Accretion Deposits (16 points), each point was analysed each 40 μm . An accelerating voltage of
204 15 kV with a beam current of 10 nA and a spot size of 5 μm were used. The counting time for
205 punctual analyses was 45 s per element; given that 5 elements could be analysed
206 simultaneously, the total time for each analysis was 90 s.

207

208 In addition, ten elements (Ca, Mg, Sr, S, Na, Mn, Fe and P) were mapped at two regions
209 with rapid accretion deposits. The EMPA mapping enables simultaneous analysis of different
210 elements and the generation of distribution maps for each element with 1 μm resolution. An
211 accelerating voltage of 20 kV with a beam current of 100 nA and a spot size and step interval of
212 1 μm diameter (dwell time = 1000 ms) were used.

213

214 **Results**

215 **Structure of *Calceola***

216 *Morphological description*

217 The specimens of *Calceola sandalina* are solitary corallum slightly curved, without
218 rootlets, with deep calices and without tabulae and dissepiments. The epithecal area in the

219 external surface has growth lines highly marked, which correspond with adult stage of ontogeny
220 and this taxon have a characteristic thick skeleton. Slipper-like external morphology highly
221 marked, with a sub-semicircular transversal section (Fig. 1). All the samples analysed lacked of
222 operculum (Fig. 1), and the study is focused in the sclerenchyma area.

223 The structure of *Calceola* is composed of a flattened and straight hingeline area with
224 protrusions (Fig. 1), formed by septa in a similar structure to articulation of strophic
225 brachiopods, although with some differences. The hingeline area, where the operculum is
226 attached, is formed by the amalgamation of major and minor septa, which sculpt fossae and
227 ridges (Fig. 1). The central septum in middle of flattened side is known as K-septum (*sensu*
228 Wright, 2010), the major septa are located generating ridges, with alar fossae at angles between
229 flat and curved sides of corallum. Major and minor septa ridges are merged toward the lumen,
230 which is almost filled by sclerenchyma. Major septa are wider than minor septa in the inner
231 surface of lumen, and all them are separated by rows of depressions (desmocyte attachment
232 scars, *sensu* Stolarski, 1993) in the interseptal space (Fig. 1). Single rows of desmocyte scars
233 only can be observed in adult samples (Wright, 2010).

234 The mode of life of *Calceola* has been discussed in numerous papers due to their unusual
235 opercular structure (Stolarski, 1993; Gudo, 1998, 2002; Galle and Ficner, 2004). Although some
236 aspects of their life style, as the current orientation and feeding, are unresolved, the position of
237 the calix over the muddy seafloor is accepted, lying on the flat side as a snowshoe (Stolarski,
238 1993; Gudo, 2002). Some authors suggest that the distal or cardinal tip of calix could be
239 partially buried in sediments and the function of operculum is protecting the polyps of predators
240 and turbulent currents, compensating the effects of sedimentation. Galle and Ficner (2004)
241 suggest that the articulation of operculum could help to the coral to move upward in the
242 sediments changing the gravitational centre of calix (Fig. 2A-C).

243

244 *Microstructural characterization*

245 *Calceola sandalina* has a complex microstructure, which is result of their complex inner
246 structuration, probably as consequence of the opercular insertion and mobility.

247 The polished slides and thin-sections show that microstructure of *Calceola* is separated in
248 three areas: K-septum, hingeline and septal apparatus (Fig. 2E-F). The different bricks that
249 compose the microstructure are lamellae, fibres and granules.

250 Several areas have been distinguished by microstructure in the hingeline: a long undulated
251 microgranular structure that separates the hingeline and the septal apparatus (Fig. 2E) crossing
252 the semispherical section of the corallum along its transverse axis; and hemispheric
253 microgranular zones (100 – 150 μm of radius) separated each c.a. 800 μm , which correspond
254 with the protrusions centres of septa (Fig. 2E-F, white arrow). Surrounding these zones appear
255 tiny microgranular lines that come from the flattened external part of the epitheca and intercept
256 the undulated microgranular zone (Fig. 2F). These lines correspond with the fossae between
257 septa and in some points the microgranular zones are cut in a triple point, where microgranular
258 hemispheric areas are developed (Fig. 2F, 3A). These microgranular deposits (undulated
259 structure, hemispheric deposits and tiny lines) are referred as Rapid Accretion Deposits (RAD)
260 throughout the text (Fig. 2).

261 On the other hand, the septal apparatus is subdivided in two microstructural areas (Fig. 2E):
262 composed-septa, which area formed by a row of major and minor septa parallels, pointing to the
263 lumen and slightly curved to the K-septum (middle area of skeleton, Figure 2F). In polished
264 sections an alternating change of coloration between septa can be observed. This area is shorter
265 in calical regions than middle regions of skeleton (Fig. 2F). Moreover, the composed-septa end
266 when the minor septa disappear, merging the major septa in a very sloped structure (Fig. 2E),
267 and this area is referred as merged septa throughout the text.

268

269 The lamellae, *sensu* Lafuste (1983), are common microcrystals present in all the areas.
270 They are straight to slightly wavy, with indentations at their edges, and are completely
271 imbricated with each other showing a compact frame (Fig. 3). The most characteristic
272 morphologies are ‘scutellate’ lamellae (Lafuste, 1983, Figure 3D), plier-shaped lamellae
273 (Lafuste, 1983, Figure 3B,E) and cupolar (dome-shaped) lamellae (Lafuste, 1981). These
274 structures are microlamellae, (< 25 μm , *sensu* Rodríguez, 1989), having a lateral development in

275 two dimensions, with lengths from 3 to 15 μm (mean = 9 μm) and width from 1 to 5 μm (mean
276 = 3 μm). In those areas where the stacking of lamellae is continuous as in the septal apparatus,
277 the morphological axis is permanently oriented perpendicular to the lumen, parallel to growth
278 direction, pointing the concave part of lamellae out to the lumen. In the hingeline the lamellae
279 show a concentric appearance (Fig. 3A) around RAD, with the concave part pointing to the
280 centre of structure.

281 K-septum is characterized by a lamellar sclerenchyma with dome-shaped lamellae, whereas
282 the composed septa and merged septa show scutellate (large and undulate appearance, Fig. 3F)
283 and plier-shaped lamellae.

284 The fibres (F) are located in the desmocyte scars, where the skeleton was projected forming
285 tepee-like structures (Fig. 3B) toward the lumen area, favouring the attachment of cells. The
286 tepee-like structures have a length of *c.a.* 100 μm . Fibres are crystals with irregular elongated
287 morphologies and indentations at their edges, which occasionally converge at their apex
288 forming needles (Fig. 3C), with a perpendicular orientation in relation to the location of the
289 skeleton. The fibres are from 8 to 23 μm (mean = 17 μm) in length and between 3 and 5 μm
290 (mean = 4 μm) in width.

291 Instead, the granules (G) are located in the Rapid Accretion Deposits (RAD) in the
292 hingeline (Fig. 3A). The granules have a length from 2 to 6 μm (mean = 3 μm) and width
293 between 2 and 4 μm (mean = 3 μm)

294 The microcrystals are structured by submicrometric lamination, which grew almost parallel
295 to morphological axis (Fig. 3D-F). They are imbricated and their morphological shapes change
296 gradually between the different skeletal elements (from granules to lamellae changing the sizes;
297 from lamellae to fibres changing the morphological axis, Figures 3A-C).

298

299 *Nanostructural characterization*

300 AFM images of *Calceola* skeleton (Figure 4) show an intricate nanostructure composed of
301 similar nanogranules in lamellae fibres and granules. The nanogranules are arranged forming
302 pill-shaped morphologies with variable sizes, 63–155 nm (mean = 105 nm) in length and 24–48

303 nm (mean = 33 nm) in width, which depends of the section. The distribution of nanocrystals
304 shows the long axis parallel to submicrometric lamination observed at microscale. This
305 intralamination is composed of laminar aggregates of nanocrystals, arranged in domains co-
306 oriented parallel to the morphological axis of microcrystals (Fig. 4C-D). In those cases where
307 two microcrystals are co-oriented, the edge between both seems a disrupted contact. The
308 nanocrystals are co-oriented in the contact points bridging the microcrystals (Fig. 4E-G). If the
309 microcrystals are misoriented (Fig. 4A-D), the nanotexture between both crystals are
310 misoriented and bridges between them cannot be observed.

311 In addition, the boundaries of the nanogranules show a dark colour in phase images,
312 indicating a different chemical composition (Figure 4H, J, L), being in some cases very thin *c.a.*
313 5 nm and diffuse (Fig. 4 H, I). Groups of nanocrystals show dark envelopes around them,
314 thicker than those observed between the nanounits (Fig. 4H). Several authors (Dauphin 2002;
315 Baronnet et al., 2008; Cuif *et al.* 2008; Gorzelak *et al.* 2013; Coronado *et al.*, 2015c; Coronado
316 and Rodríguez, 2015) have studied these envelopes in recent and fossil organisms and proposed
317 that they could be organic coatings from the original organic matrix with amorphous calcium
318 carbonate (ACC) remaining.

319

320 **Crystallography of *Calceola***

321 The location of the c-axis orientation images of (CIP) and the EBSD maps are positioned in
322 the Figure 2.

323 *CIP (mesoscale):*

324 Computer-integrated-polarization microscopy (CIP) has been used with the purpose of
325 identify the crystallographic arrangement of the skeleton at mesoscale. Three c-axis orientation
326 images (COI) of a transversal section and their corresponding pole-figures were obtained using
327 the CIP method from different parts: one in the composed septa and two in the hingeline area.
328 The purpose was to analyse the relationship between the RAD undulate and the insertion of
329 septa (Fig. 5A-B) and the relationship between the hemispherical RAD and the surrounding
330 lamellar sclerenchyma (Fig. 5E-F).

331 The crystallographic data of CIP reveal a complex architecture. The c-axis is perpendicular
332 to morphological axis in lamellae, and parallel in fibres, whereas the granules, and those
333 transitional lamellae (more rounded) formed around of RAD, show a c-axis almost orthogonal
334 to the structure. The c-axis orientation of the sclerenchyma is opposite in the hingeline side
335 versus the septal apparatus. In the case of the microcrystals beyond the hingeline (septal
336 apparatus) the c-axis points toward the lumen, but the microcrystals at the hingeline, exhibit a
337 complex orientation constantly modified by the RAD, pointing to outside the c-axis of lamellae
338 at the edge of coral (epitheca).

339 The mean inclination of c-axis is *c.a.* 35° in lamellae in the septal insertion of the hingeline
340 area (Fig. 5A-B). Although the azimuthal dispersion is great, *c.a.* 90° as a result of the rotation
341 around RAD area, most crystals are grouped in two pole maxima at *c.a.* 50° and the orientation
342 and morphological axis exhibit an undulate trajectory between septa. The region I (Fig. 5)
343 shows the punctual orientation of all pixels in the RAD zone, exhibiting a high inclination of c-
344 axis *c.a.* 75° and a surrounded azimuthal distribution focused in two pole maxima completely
345 opposite. The c-axis inclination of the orientation image (Fig. 5A-B) shows that RAD undulate
346 line is discontinuous but exhibits the same inclination in all of scattered deposits.

347 During the advance of septa to the lumen, the composed-septa exhibit a more controlled c-
348 axis orientation, with less azimuthal dispersion (Fig. 5C-D). The studied area shows a twist of
349 the lamellae sclerenchyma favoured by the union of septa, showing a wavy structure and
350 orientation (Fig. 5C-D). The azimuthal dispersion is constricted to *c.a.* 40° and the inclination
351 varies depending on the side of septum, between *c.a.* 25° to 60°.

352 In the area of hemispheric RAD, the lamellae surround the microgranular zone, rotating
353 each *c.a.* 15°. The mean inclination is *c.a.* 30°, similar to other areas, but as it approaches to the
354 RAD the lamellae are more inclined *c.a.* 55° and an azimuthal dispersion of *c.a.* 40° in the area
355 II, to *c.a.* 70° of inclination and azimuthal dispersion in the area III. The orientation image
356 shows a large irregular ellipsoidal area around the RAD, where the lamellar sclerenchyma is
357 highly inclined. This area can be observed in the polished sections with different coloration
358 (Fig. 2E,F).

359

360 *EBSD (microscale):*

361 Six EBSD maps have been drawn in two different transversal sections of *Calceola*
362 skeleton: three of them correspond with the composed septa area, one was done in the inner of
363 K-septum, one was done in the inner of a hemispheric RAD and the last one was done in
364 merged septa area.

365 The analyses with EBSD confirm that the composition of *Calceola* is only calcite, without
366 traces of other carbonates, as was observed with petrographic microscopy and CIP. Each
367 microcrystal have a pole maxima in the planes $\{10\bar{1}0\}$ and $\{10\bar{1}4\}$ characteristics of trigonal
368 symmetry of calcite.

369 Crystallographic maps show the fibres and granules behaves like a single crystal (Fig. 6C-
370 D, 7), the morphology of crystal is clearly defined by the index intensity images by means of the
371 quality of diffraction of each crystal and the crystallographic orientation maps exhibit individual
372 orientations for each microcrystal. In the case of lamellae, most of them behave as single
373 crystals but some of them have composed-crystals features as can be seeing as in the plier-
374 shaped lamellae (Fig. 6E-F). The index intensity images reveal different subcrystals forming the
375 composed-crystal (fig. 6E). In misoriented crystals the none-diffraction areas are continuous and
376 thick, whereas between co-oriented crystals and in the inner of composed-crystals are dashed.

377 The c-axis orientation varies with respect to the morphological axis between each
378 crystallographic element; perpendicular in lamellae, parallel in fibres and almost vertical in
379 granules.

380 Diffraction maps of composed-septa zone (Fig. 6A-B) show well defined crystals with
381 microlamellae morphology imbricated composing a frame. The plane $\{0001\}$ exhibits a pole
382 maximum with a dispersion of *c.a.* 40° and an inclination *c.a.* 30° . The planes $\{10\bar{1}0\}$ and
383 $\{01\bar{1}0\}$ shows a rotation of a- and b-axes around c-axis each *c.a.* 15° and an inclination of axis
384 of *c.a.* 40° (Fig. 6I-II). Orientation distribution function (ODF) of the $\{10\bar{1}4\}$ plane confirm the
385 rotation of a- and b-axes, showing an irregular turbostratic distribution (Fig. 6).

386 These features vary along the composed-septa, *e.g.* in those areas where the fibres appear,
387 which correspond with desmocyte scars (Fig. 6C-D). These areas are characterised by a
388 protrusion of the septum forming an attachment structure with the desmocyte cells. The fibres
389 appear as tepee-like structures and the crystallographic orientation vary from the lamellar
390 sclerenchyma to the tepee-like *c.a.* 85°. Two different areas have been observed: one with part
391 of the crystals rotating *c.a.* 60° with an inclination of *c.a.* 40° and other cluster of crystals with
392 an inclination of *c.a.* 15° and a rotation of *c.a.* 35° but with a gradual rotation of the c-axis
393 between two clusters (Fig. 6IV-V). The pole figure and ODF figures, in the planes $\{10\bar{1}0\}$ and
394 $\{10\bar{1}4\}$, show a complex arrangement with a rotation each *c.a.* 45° of a- and b-axes.

395 On the other hand, the merged septa area shows a high ordered crystallography. The Figure
396 A1A-B, shows a fusion area between two major septa (green colorations) and a minor septa
397 (purple coloration). The c-axis shows a rotation between septa of *c.a.* 55°, and an inclination of
398 *c.a.* 30° in lamellae (Fig. A1,I-II). The planes $\{10\bar{1}0\}$ and $\{10\bar{1}4\}$ show a rotation of a- and b-
399 axes of *c.a.* 60° without turbostratic distribution (Fig. A1,III).

400 In the case of K-septum map, the EBSD data reveal a microstructure slightly ordered with a
401 pole maxima in the plane $\{0001\}$ but broadly disperse, and a variation of inclination of *c.a.* 30°
402 (Fig.A1C-D). The planes $\{10\bar{1}0\}$ and $\{10\bar{1}4\}$ show a turbostratic distribution of a- and b-axes
403 rotating *c.a.* 20° around c-axis (Fig. A1,VI).

404 In contrast to the previously shown, RAD show a microgranular texture (Fig. 7), composed
405 by rounded granules with thick none-diffraction areas around them. The crystallographic grains
406 reveal that the granules exhibit a pole maxima in the $\{0001\}$ plane with an inclination *c.a.* 70°,
407 and a rotation of a- and b-axes represented in the pole figures and ODF figures of *c.a.* 30° (Fig.
408 7I-III). The index intensity image shows that diffraction increases toward outside the RAD, and
409 the crystallographic arrangement is more ordered (Fig. 7A).

410 The misorientation histograms show that the correlated and uncorrelated misorientation
411 differs between the different zones studied, although some zones have similar distributions (Fig
412 A2). The common features in the composed septa, merged septa and RAD have a main mode at
413 5°, indicating the co-orientation of microcrystals and highly ordered structures. On the contrary,

414 the area of composed-septa with desmocyte scars shows a less ordered crystallography, with a
415 distribution centred at the mode 45° and high misorientation angles (e.g. 85°). In the case of
416 merged septa the histogram describes a double distribution with two modes, one to 15° - 20° and
417 other to 55° , the last one could be derived of the fusion of septa and their disorientation. K-
418 septum misorientation exhibit an almost normal distribution centred at 40° - 45° in agreement
419 with the broad dispersion at the plane $\{0001\}$.

420 **Geochemistry**

421 The chemical composition of the rapid accretion deposits (RAD) was evaluated by EMPA
422 mapping (Fig. 8) in one area, and the chemical composition of skeleton thorough 116 random
423 points of analysis of nine elements (Ca, Mg, Sr, S, Ba, Na, Mn, Fe and P) in a transversal
424 section. Only six elements (Ca, Mg, Sr, Na and S) and backscatter electron images (BSE) have
425 been represented in the Figure 8, because show representatives changes in that area.
426 Additionally, two transverse lines of RAD were analysed (16 points) to check the geochemical
427 internal variation within the structure (Fig. 9A-B, represents one of them). Table 1 summarises
428 the EMPA analyses for all the elements. The values of EMPA analysis were normalised to mol
429 % of CaCO_3 , MgCO_3 , SrCO_3 , MnCO_3 and FeCO_3 , whereas the values of S, Na, Ba and P were
430 given as ppm.

431 The BSE images (Fig, 8A, G, Fig. 9B) show a homogenous composition of the lamellar
432 sclerenchyma, whereas the RAD structure is clearly visible by the variation in its brightness.
433 The grey scale variation of the BSE image depends mainly on the atomic number of elements at
434 each point. Levels of Ca (Fig.8B) are decreased in the RAD, delimiting a circular structure and
435 some isolated spots around the structure exhibit a special decline of the Ca amount. This
436 variation has a co-variation with the Mg levels, which increase in these areas with regard to the
437 lamellae. It should be noted that some isolated points show high amounts of Mg (Fig. 8C,H).
438 These points match with black dots in BSE. The mol % of $\text{MgCO}_3/\text{CaCO}_3$ have been plotted,
439 exhibiting a linear correlation ($R^2 = 0.96541$). This linear correlation indicates these elements
440 are located at the same spaces in the lattice of CaCO_3 . The MgCO_3 mean value in the corals is

441 2.39 mol % (Table 1), far below of the lower limit of high magnesium calcite (HMC), at 4 mol
442 % of MgCO₃.

443 Sr and Na distributions are homogeneous except in some isolated areas. Sr seems to be
444 more centred around RAD (Fig. 8D-E), in contrast with Na which seems to be centred in
445 isolated points in the inner part of RAD, although values are lower than the detection limit
446 (Table 1). Noteworthy the inner area of RAD show higher values of S with regard to the
447 lamellar sclerenchyma, which exhibits a homogeneous distribution of S (Fig. 8F,I). The Ba and
448 P value are not statistically representative and in many points its quantity is below the detection
449 limit of the spectrometer. The Fe and Mn are elements indicative of diagenetic alteration,
450 replacing the Mg with Fe and Mn (Barbin, 2013; Coronado *et al.*, 2013; Coronado *et al.*,
451 2015c). The values of these elements are very low in coral skeleton and homogeneous, except
452 isolated points, not indicating diagenetic alteration (Table 1).

453 The analyses of transverse line (Fig. 9A) show that the values of Mg are increased with
454 regard of Ca in the RAD area. S exhibit a slight rising in the RAD, but the maximum values not
455 match with the Mg. Moreover, Sr exhibits a decrease in the RAD and a slight increase in the
456 limits of structure.

457

458 **Discussion and conclusions**

459 The structural, crystallographic and geochemistry study reveals that *Calceola* skeletons are
460 hierarchical structures formed by low magnesium calcite crystals with a high degree of self-
461 assembly. The microstructural elements show gradual transition between them and the different
462 specialized areas, which is common characteristic in Palaeozoic corals (Coronado *et al.*, 2013,
463 2015a). The different crystalline bricks that form the microstructure (lamellae, fibres and
464 granules) are imbricated and their morphological shape change gradually between the different
465 areas of skeletal elements (hingeline, septal apparatus).

466 The microcrystals are composed of co-oriented nanocrystals that remind to mesocrystals
467 (Cölfen and Antonietti, 2005). Observations at atomic scale (with AFM and TEM, Cuif and

468 Dauphin, 2005; Stolarski, 2003; Janiszewska *et al.*, 2011) have demonstrated that the
469 biocrystallization occur by particle attachment (CPA, *sensu de Yoreo et al.*, 2015) in
470 biominerals, including recent corals (Cuif *et al.*, 2012). The nanoscale observations in *Calceola*
471 suggest a crystallization process similar to CPA, by the attachment of nanogranules with pill-
472 shaped co-oriented forming a microcrystal. Apparently the pathway of crystallization cannot be
473 solved with our fossil data, but some evidences suggest that the Palaeozoic corals, including
474 *Calceola* skeleton, could have grown by a stepped coordinated-growth mode as described in
475 scleractinians and molluscs by Cuif *et al.* (2012) and also in Syringoporicae by Coronado *et al.*
476 (2015a) and Coronado and Rodríguez (2015): 1) Attachment of nanocrystals and their
477 arrangement in sub-micrometric laminae (Fig.3D-F,4 J-L) by CPA, controlled by and organic
478 hydrogel. 2) Stacking of submicrometric laminae and the subsequent formation of microcrystals
479 (Fig.3,4), controlled by the intercrystalline organic matrix. 3) Organization in higher skeletal
480 structures as septa (Fig.5C-D), will be controlled by genetic code. The discontinuous contact of
481 nanocrystals when two microcrystals are co-oriented (Fig.4H, 6E-F) may indicate a growth of
482 microcrystals similar to mineral bridges (Checa, 2011), and the dashed none-diffraction areas
483 inside of composed grains as plier-shaped microcrystals support this hypothesis (Fig. 6-F).
484 Similar results were found in Syringoporicae (Coronado and Rodríguez, 2015)

485 The structure of *Calceola* is a dense microstructure comparable to a dendrite-like structure.
486 Similar data have been reported in Syringoporicae (Coronado *et al.*, 2015a), regarding to the
487 interdigitated growth alike to described by Goetz *et al.* (2011) in primary layer of brachiopods,
488 named 3D-jigsaw structure. This structure needs a complex organic structuration, which defines
489 the dendrite-like structure by mean membranes, or by deposition of vesicles filled with the
490 precursor of CaCO₃ in each place of biocrystallization Goetz *et al.* (2011); unfortunately the
491 data presented here cannot evidence this process.

492 The new crystallographic evidences of *Calceola* show that the epithelial tissue should be
493 almost in contact with the biocrystallization area because the skeletal structures shows high
494 crystallographic arrangement, as result of the control exerted during biocrystallization. This is a
495 common feature with other Palaeozoic corals, as Syringoporicae (Coronado and Rodríguez,

496 2015). Like the turbostratic distribution in some of skeletal areas, this is lost in complex
497 microstructural areas as desmocyte scars. Probably this feature is an inherited character of other
498 cylindrical Palaeozoic corals (Coronado *et al.*, 2015a) being more easy observable in the well
499 organised areas as the composed-septa. However the concentrically distribution of
500 microcrystalline domains of Syringoporicae (Coronado *et al.*, 2013; Coronado *et al.*, 2015a,b) is
501 not represented in *Calceola*, as result of their complex inner structuration and the merging of
502 their septal apparatus.

503 *Calceola* skeleton shows a great crystallographic organization being higher in the merged
504 septa than in the hingeline area. The hingeline area is characteristic by their complex
505 microstructure, highlighting the presence of Rapid Accretion Deposit (RAD) on it. These
506 deposits have a diverse morphology, which depends on the position in the skeleton. The RAD in
507 the hingeline separates two areas with opposite c-axis orientation (septal apparatus and
508 hingeline).

509 As occur in Syringoporicae and other calcitic groups of animals, (brachiopods and
510 molluscs) the crystallographic arrangement of the skeletons show a distribution and
511 misorientation that would prevent skeleton fracture by cleavage. Calcite crystals are easily
512 cleaved on their $\{10\bar{1}4\}$ planes (Schmahl *et al.* 2004; Pérez-Huerta *et al.*, 2007). The skeletons
513 of *Calceola* have the c-axis oriented perpendicular to the growth direction around the lumen,
514 except in the hingeline, where the c-axis is almost similar to growth direction. Coronado *et al.*
515 (2015a) established that the circular variation of c-axis around skeleton in Syringoporicae
516 protects against fracture from lateral currents of seawater and the turbostratic distribution could
517 be a strategy to prevent cleavage. In the case of *Calceola* the disorientation of c-axis in the
518 bottom-side, probably is related with the mechanical effort of hingeline area during the
519 movement of the operculum for example when the coral was being retracted.

520 A remarkable structure present in *Calceola* is Rapid Accretion Deposits (RAD), which
521 remind to RAD of scleractinian. RAD in scleractinian are deposits composed of very fine
522 granular crystals forming occasionally hemispheric structures, which are surrounded by
523 isometric aragonitic fibres, shorter at the beginning. A high concentration of organic phases at

524 the centre of RAD is common (Stolarski, 2003, Cuif *et al.*, 2012; Janiszewska *et al.*, 2015). On
525 the other hand, these isometric aragonitic fibres are arranged in thin layers and individual
526 bundles of fibres, composing a compact zone, densely banded with less organic phases present
527 on them, forming the Thickening Deposits (TD, Stolarski, 2003; Janiszewska *et al.*, 2015). The
528 RAD are enriched, in contrast with the TD, in several elements as a response to ‘vital effects’;
529 Mg, Sr, S and Ba (Cuif *et al.*, 2003; 2012; Meibom *et al.*, 2004, 2008), whereas several isotope
530 ratios, such as $d^{13}\text{C}$, $d^{18}\text{O}$, and $d^{11}\text{B}$, are depleted in RAD (Holocomb *et al.*, 2009). The
531 enhancement in S and Mg has been associated with organic phases of organic matrix (which is
532 composed by carbohydrates, proteins and lipids Dauphin *et al.*, 2008, Cuif *et al.*, 2011). The S is
533 found mainly as sulphated polysaccharides (Cuif *et al.*, 2003; Cuif and Dauphin, 2005; Dauphin
534 *et al.*, 2008, Cusak *et al.*, 2008) and the Mg is introduced by a disordered Mg-bearing, which
535 could be accommodated in organic phases or in a highly disordered inorganic phase (Finch and
536 Allison, 2008). On the other hand, the RAD are nucleated quickly during the biocrystallization
537 (Domart-Coulon *et al.*, 2014), and probably the high concentrations of organic phases help to
538 stabilise the CaCO_3 deposits during the fast growth.

539 The RAD in *Calceola* are enriched in Mg, S, and slightly in Sr in the edges of structure.
540 The microstructure of these hemispheric deposits has a granular microstructure that changes to
541 lamellae laterally, modifying the morphology and size of crystals, in a similar way to
542 scleractinian. Besides, RAD in *Calceola* are located in areas of fast development, as the ridges
543 of the hingeline area, responsible for the operculum closure. These data support the idea that the
544 Rapid Accretion Deposits (RAD) of *Calceola* were a convergent structure with other cnidarians
545 and their biocrystallization processes could be analogous.

546 On the other hand, Lafuste and Semenov-Tian-Chansky (1968) described a system of tubes
547 along of *Calceola* skeleton in other skeletons from Smara (Morocco, old Spanish Sahara). They
548 found that these tubes, named ‘canalicules’, cross longitudinally the *Calceola* skeleton, near to
549 external perimeter in the hingeline area. Lafuste and Semenov-Tian-Chansky (1968) indicated a
550 maximum diameter of 0.17 mm and a vertical spacing of generally 0.7-0.8, varying from 0.5-1
551 mm for the tubes. These features and their location in the structure suggest that the ‘canalicules’

552 described by Lafuste and Semenov-Tian-Chansky (1968) could be part of the hemispheric RAD
553 , which are structures of 100-150 μm of diameter and 800 μm of spacing. Lafuste and
554 Semenov-Tian-Chansky (1968) and Wright (2010) suggest that these tubes are filled with clear
555 calcite. Although the biological significance of tubes is unknown, some authors have offered a
556 hypothesis: Pedder *et al.* (1998) highlight that these tubes have not found in other corals and
557 that they could be produced by commensal organisms. Wright (2010) rejects the commensalism
558 idea and suggests that they could be part of the specialised muscles for the closing system of
559 operculum. The new data reported here support the idea that these tubes described by Lafuste
560 and Semenov-Tian-Chansky (1968) could be a diagenetic artefact of the recrystallization of
561 RAD, by dissolution of granules and sparite co-precipitation.

562 On the other hand, the RAD are composed of granules forming hemispheric structures in
563 aggregates, which look opaque areas in transmitted light derived of stacking of crystals, similar
564 to scleractinian. The Lafuste and Semenov-Tian-Chansky (1968) descriptive observations of
565 ‘canalicules’ system point to a similar hemispheric structures described in the RAD of septal
566 areas of deep-water corals as *Desmophyllum* (Stolarski, 2003) and micrabaciids (Janiszewska *et*
567 *al.*, 2011). Although the recrystallized RAD of Lafuste and Semenov-Tian-Chansky (1968)
568 have a concave base instead of the convex base of recent scleractinian.

569 Lafuste (1983) differentiated *Calceola* from Goniophyllidae by the microstructure, as
570 explain above. The microstructural data provided by petrographic microscopy and EBSD in this
571 study show dome-shaped microcrystals at the skeleton of *Calceola* in K-septum mainly. These
572 microcrystals are common in Goniophyllum and *Calceola* suggesting that these two groups are
573 not separated and they should be part of Goniophyllidae as grouped Hill (1991). Stolarski
574 (1993) proposed a phylogenetic lineage between these groups and the parent group Cothoniida
575 (Cambrian, Korde, 1963) based in their morphological similarities in early stages of growth.
576 The crystallo-chemical features of this basal group should be analysed to enlighten the origin of
577 Palaeozoic corals.

578 The features described in this study suggest common biocrystallization processes between
579 different cnidarians (Tabulata, Rugosa and Scleractinian) at nano- and microscale. The
580 crystallo-chemical features of Palaeozoic corals are most dissimilar to the scleractinians
581 probably as result of their mineralogy and phylogenetic origin, but some common
582 characteristics in the two groups of corals suggest analogous processes of biomineralization
583 derived from a stem group of cnidarians. The results of this paper highlight the value of
584 biomineralization studies in fossil organisms to understand the evolution of biomineralization
585 mechanism through Phanerozoic.

586

587 **Acknowledgements**

588 Financial support through the Spanish Ministerio de Economía y Competitividad (research
589 project CGL2012-30922BTE) and Complutense University Research Group (910231) is
590 gratefully acknowledged. Ismael Coronado acknowledges financial support through a Synthesis
591 grant (FR-TAF-2397) developed in MNHN (Paris, France) during 2012, which allowed
592 studying the material of Lafuste's collection. We thank the anonymous reviewers and the editor
593 (Claro Ignacio Sáinz-Díaz) for their help and constructive comments on the text.

594 **References:**

595

596 **Bachmann**, F., Hielscher, R., Schaeben, H., 2011. Grain detection from 2d and 3d EBSD
597 data—Specification of the MTEX algorithm. *Ultramicroscopy* 111, 1720-1733.

598 **Balthasar**, U., Cusack, M., Faryma, L., Chung, P., Holmer, L.E., Jin, J., Percival, I.G.,
599 Popov, L.E., 2011. Relic aragonite from Ordovician–Silurian brachiopods: Implications for the
600 evolution of calcification. *Geology* 39, 967-970.

601 **Barbin**, V., 2013. Application of cathodoluminescence microscopy to recent and past
602 biological materials: a decade of progress. *Mineralogy and Petrology* 107, 353-362.

603 **Barbin**, V., Ramseyer, K., Elfman, M., 2008. Biological record of added manganese in
604 seawater: a new efficient tool to mark in vivo growth lines in the oyster species *Crassostrea*
605 *gigas*. International Journal of Earth Sciences 97, 193-199.

606 **Barret**, S., 1997. Image analysis and the internet Scientific Data Management 1, 18-25.

607 **Benedix**, G., Jacob, D.E., Taylor, P.D., 2014. Bimineralic bryozoan skeletons: a comparison
608 of three modern genera. Facies 60, 389-403.

609 **Checa**, A., Jiménez-López, C., Rodríguez-Navarro, A., Machado, J., 2007a. Precipitation of
610 aragonite by calcitic bivalves in Mg-enriched marine waters. Marine Biology 150, 819-827.

611 **Checa**, A.G., Esteban-Delgado, F.J., Rodríguez-Navarro, A.B., 2007b. Crystallographic
612 structure of the foliated calcite of bivalves. J Struct Biol 157, 393-402.

613 **Checa**, A.G., Cartwright, J.H.E., Willinger, M.-G., 2011. Mineral bridges in nacre. Journal
614 of Structural Biology 176, 330-339.

615 **Coronado**, I., Rodríguez, S., 2015. Biomineral structure and crystallographic arrangement of
616 cerioid and phaceloid growth in corals belonging to the Syringoporicae (Tabulata, Devonian–
617 Carboniferous): a genetic reflection. Geological Magazine, 1-25.

618 **Coronado**, I., Pérez-Huerta, A., Rodríguez, S., 2013. Primary biogenic skeletal structures in
619 *Multithecopora* (Tabulata, Pennsylvanian). Palaeogeography, Palaeoclimatology, Palaeoecology
620 386, 286-299.

621 **Coronado**, I., Pérez-Huerta, A., Rodríguez, S., 2015a. Crystallographic orientations of
622 structural elements in skeletons of Syringoporicae (tabulate corals, Carboniferous): implications
623 for biomineralization processes in Palaeozoic corals. Palaeontology 58, 111-132.

624 **Coronado**, I., Pérez-Huerta, A., Rodríguez, S., 2015b. Computer-integrated polarisation
625 (CIP) in the analysis of fossils: a case of study in a Palaeozoic coral (*Sinopora*, Syringoporicae,
626 Carboniferous). Historical Biology 27, 1098-1112.

627 **Coronado**, I., Fernández-Martínez, E., Rodríguez, S., Tourneur, F., 2015c. Reconstructing a
628 Carboniferous inferred coral–alcyonarian association using a biomineralogical approach.
629 Geobiology 13, 340-356.

630 **Cuif**, J.-P., 2014. The Rugosa–Scleractinia gap re-examined through microstructural and
631 biochemical evidence: A tribute to H.C. Wang. *Palaeoworld* 23, 1-14.

632 **Cuif**, J.-P., Dauphin, Y., 2005. The two-step mode of growth in the scleractinian coral
633 skeletons from the micrometre to the overall scale. *Journal of Structural Biology* 150, 319-331.

634 **Cuif**, J.-P., Dauphin, Y., Sorauf, J.E., 2011. *Biomaterials and fossils through time* Cambridge
635 University Press, Cambridge; New York.

636 **Cuif**, J.-P., Dauphin, Y., Doucet, J., Salomé, M., Susini, J., 2003. XANES mapping of
637 organic sulfate in three scleractinian coral skeletons. *Geochimica et Cosmochimica Acta* 67, 75-
638 83.

639 **Cuif**, J.-P., Dauphin, Y., Nehrke, G., Nouet, J., Perez-Huerta, A., 2012. Layered Growth and
640 Crystallization in Calcareous Biomaterials: Impact of Structural and Chemical Evidence on Two
641 Major Concepts in Invertebrate Biomaterialization Studies. *Minerals* 2, 11-39.

642 **Cuif**, J.P., Dauphin, Y., Farre, B., Nehrke, G., Nouet, J., Salomé, M., 2008. Distribution of
643 sulphated polysaccharides within calcareous biomaterials suggests a widely shared two-step
644 crystallization process for the microstructural growth units. *Mineralogical Magazine* 72, 233-
645 237.

646 **Cusack**, M., Dauphin, Y., Cuif, J.-P., Salomé, M., Freer, A., Yin, H., 2008. Micro-XANES
647 mapping of sulphur and its association with magnesium and phosphorus in the shell of the
648 brachiopod, *Terebratulina retusa*. *Chemical Geology* 253, 172-179.

649 **Dauphin**, Y., 2002. Fossil organic matrices of the Callovian aragonitic ammonites from
650 Lukow (Poland): location and composition. *International Journal of Earth Sciences* 91, 1071-
651 1080.

652 **Dauphin**, Y., Cuif, J.-P., Williams, C.T., 2008. Soluble organic matrices of aragonitic
653 skeletons of Merulinidae (Cnidaria, Anthozoa). *Comparative Biochemistry and Physiology Part*
654 *B: Biochemistry and Molecular Biology* 150, 10-22.

655 **De Yoreo**, J.J., Gilbert, P.U., Sommerdijk, N.A., Penn, R.L., Whitlam, S., Joester, D.,
656 Zhang, H., Rimer, J.D., Navrotsky, A., Banfield, J.F., 2015. Crystallization by particle
657 attachment in synthetic, biogenic, and geologic environments. *Science* 349, aaa6760.

658 **Domart-Coulon**, I., Stolarski, J., Brahmi, C., Gutner-Hoch, E., Janiszewska, K., Shemesh,
659 A., Meibom, A., 2014. Simultaneous extension of both basic microstructural components in
660 scleractinian coral skeleton during night and daytime, visualized by in situ ⁸⁶Sr pulse labeling.
661 Journal of Structural Biology 185, 79-88.

662 **Ezaki**, Y., 1998. Paleozoic Scleractinia: progenitors or extinct experiments? Paleobiology
663 24, 227-234.

664 **Finch**, A.A., Allison, N., 2008. Mg structural state in coral aragonite and implications for the
665 paleoenvironmental proxy. Geophysical Research Letters 35.

666 **Galle**, A., Ficner, F., 2004. Middle Devonian *Calceola sandalina* (Linnaeus,
667 1771)(Anthozoa, Rugosa) from Moravia (Czech Republic): aspects of functional morphology,
668 gerontic growth patterns, and epibionts. Geodiversitas 26, 17-31.

669 **Goetz**, A.J., Steinmetz, D.R., Griesshaber, E., Zaefferer, S., Raabe, D., Kelm, K., Irsen, S.,
670 Sehrbrock, A., Schmahl, W.W., 2011. Interdigitating biocalcite dendrites form a 3-D jigsaw
671 structure in brachiopod shells. Acta Biomaterialia 7, 2237-2243.

672 **Gorzalak**, P., Stolarski, J., Mazur, M., Meibom, A., 2013. Micro- to nanostructure and
673 geochemistry of extant crinoidal echinoderm skeletons. Geobiology 11, 29-43.

674 **Gudo**, M., 1998. The soft body of *Calceola sandalina*: summary of morphological
675 reconstruction, function, ontogeny, and evolutionary history. Newsletter of Fossil Cnidaria &
676 Porifera 27 (1), 21-26.

677 **Gudo**, M., 2002. Structural–functional Aspects in the Evolution of Operculate Corals
678 (Rugosa). Palaeontology 45, 671-687.

679 **Heilbronner**, R., Barret, S., 2014. Image Analysis in Earth Sciences - Microstructures and
680 Textures of Earth Materials Springer, London.

681 **Hill**, D., Jell, J., 1969. On the rugose coral genera *Rhizophyllum* Lindström, *Platyphyllum*
682 Lindström and *Calceola* Lamarck. Neues Jahrbuch für Geologie und Paläontologie,
683 Monatshefte 9, 534-551.

684 **Holcomb**, M., Cohen, A.L., Gabitov, R.I., Hutter, J.L., 2009. Compositional and
685 morphological features of aragonite precipitated experimentally from seawater and biogenically
686 by corals. *Geochimica et Cosmochimica Acta* 73, 4166-4179.

687 **Horcas**, I., Fernández, R., Gómez-Rodríguez, J.M., Colchero, J., Gómez-Herrero, J., Baro,
688 A., 2007. WSXM: a software for scanning probe microscopy and a tool for nanotechnology.
689 *Review of Scientific Instruments* 78, 8.

690 **Jakubowicz**, M., Berkowski, B., Correa, M.L., Jarochovska, E., Joachimski, M., Belka, Z.,
691 2015. Stable Isotope Signatures of Middle Palaeozoic Ahermatypic Rugose Corals—Deciphering
692 Secondary Alteration, Vital Fractionation Effects, and Palaeoecological Implications. *PLoS*
693 *ONE* 10, e0136289.

694 **Janiszewska**, K., Stolarski, J., Kitahara, M.V., Neuser, R.D., Mazur, M., 2015.
695 Microstructural disparity between basal micrabaciids and other Scleractinia: new evidence from
696 Neogene Stephanophyllia. *Lethaia* 48, 417-428.

697 **Janiszewska**, K., Stolarski, J., Benzerara, K., Meibom, A., Mazur, M., Kitahara, M.V.,
698 Cairns, S.D., 2011. A unique skeletal microstructure of the deep-sea micrabaciid scleractinian
699 corals. *Journal of Morphology* 272, 191-203.

700 **Korde**, K.B., 1963. Hydroconozoa, a new class of Coelenterata. *Paleontologicheskii*
701 *Zhurnal*, 20-25.

702 **Kowalski**, H., 1983. Die pantoffelkoralle *Calceola sandalina*. *Die Eigel* 78, 24-27.

703 **Kunth**, A., 1869. Beiträge zur Kenntnis fossiler Korallen. 2: Das Wachstumsgesetz der
704 Zoantharia Rugosa and über *Calceola sandalina*. *Ztschr. Dt. geol. Ges* 2, 647-687.

705 **Lafuste**, J., 1970. Lames ultra-minces a faces polies. Procède et application la
706 microstructure des Madreporaires fossiles. *Comptes rendus hebdomadaires des seances de*
707 *l'Academie des Sciences Paris* 270, 679-681.

708 **Lafuste**, J., 1981. Structure et microstructure de *Dendropora* Michelin 1846 (Tabulata,
709 Devonien). *Bulletin De La Societe Geologique De France* 23, 271-277.

710 **Lafuste**, J., 1983. Disparite microstructurale entre *Calceola* Lamarck et *Goniophyllum*
711 *Dybowski* (Tetracoralla, Devonien et Silurien). *Comptes Rendus des Seances de l'Academie des*

712 Sciences, Serie 2: Mecanique Physique, Chimie, Sciences de l'Univers, Sciences de la Terre
713 296, 1749-1752.

714 **Lafuste, J., Semenoff-Tian-Chansky, P., 1968.** Présence d'un système de canalicules dans le
715 squelette de *Calceola* Lamarck. CR Acad. Sci. Paris 267, 1139-1141.

716 **Lafuste, J., Plusquellec, Y., 1985.** Attribution de "*Michelinia*" *compressa* Michelin, 1847 au
717 genre *Yavorskia* Fomitchev (Tabule, Tournaisien). Geobios 18, 381-387.

718 **Lafuste, J., Debrenne, F., Gandin, A., Gravestock, D., 1991.** The oldest tabulate coral and
719 the associated archaeocyatha, Lower Cambrian, Flinders Ranges, South Australia. Geobios 24,
720 697-718.

721 **Lee, M.R., Torney, C., Owen, A.W., 2012.** Biomineralisation in the Palaeozoic oceans:
722 Evidence for simultaneous crystallisation of high and low magnesium calcite by phacopine
723 trilobites. Chemical Geology 314–317, 33-44.

724 **Lindstroem, G., 1882.** Om de palaeozoiska formationernas oper kelbärende koraller PA
725 Norstedt & Söner.

726 **Lowenstam, H., Weiner, S., 1989.** On biomineralization Oxford University Press, New
727 York.

728 **Macintyre, I.G., Bayer, F.M., Logan, M.A.V., Skinner, H.C.W., 2000.** Possible vestige of
729 early phosphatic biomineralization in gorgonian octocorals (Coelenterata). Geology 28, 455-
730 458.

731 **Mann, S., 2001.** Biomineralization: Principles and concepts in bioinorganic materials
732 chemistry Oxford University Press, Oxford.

733 **Marin, F., Le Roy, N., Marie, B., Ramos-Silva, P., Bundeleva, I., Guichard, N., Immel, F.,
734 2014.** Metazoan calcium carbonate biomineralizations: macroevolutionary trends – challenges
735 for the coming decade. Bulletin de la Societe Geologique de France 185, 217-232.

736 **McAllister, J.E., Brand, U.W.E., 1989.** Primary and diagenetic microstructures in trilobites.
737 Lethaia 22, 101-111.

738 **Medina**, M., Collins, A.G., Takaoka, T.L., Kuehl, J.V., Boore, J.L., 2006. Naked corals:
739 Skeleton loss in Scleractinia. Proceedings of the National Academy of Sciences 103, 9096-
740 9100.

741 **Meibom**, A., Cuif, J.-P., Houlbreque, F., Mostefaoui, S., Dauphin, Y., Meibom, K.L.,
742 Dunbar, R., 2008. Compositional variations at ultra-structure length scales in coral skeleton.
743 Geochimica et Cosmochimica Acta 72, 1555-1569.

744 **Meibom**, A., Cuif, J.P., Hillion, F., Constantz, B.R., Juillet-Leclerc, A., Dauphin, Y.,
745 Watanabe, T., Dunbar, R.B., 2004. Distribution of magnesium in coral skeleton. Geophysical
746 Research Letters 31.

747 **Mutvei**, H., 1997. Siphuncular structure in Ordovician endocerid cephalopods. Acta
748 Palaeontologica Polonica 42, 375-390.

749 **Oliver Jr**, W.A., 1980. The relationship of the scleractinian corals to the rugose corals.
750 Paleobiology, 146-160.

751 **Pérez-Huerta**, A., Cusack, M., 2009. Optimizing Electron Backscatter Diffraction of
752 Carbonate Biominerals-Resin Type and Carbon Coating. Microscopy and Microanalysis 15,
753 197-203.

754 **Pérez-Huerta**, A., Cusack, M., England, J., 2007. Crystallography and diagenesis in fossil
755 Craniid brachiopods. Palaeontology 50, 757-763.

756 **Pérez-Huerta**, A., Cusack, M., McDonald, S., Marone, F., Stampanoni, M., MacKay, S.,
757 2009. Brachiopod punctae: A complexity in shell biomineralisation. Journal of Structural
758 Biology 167, 62-67.

759 **Porter**, S.M., 2010. Calcite and aragonite seas and the de novo acquisition of carbonate
760 skeletons. Geobiology 8, 256-277.

761 **Rahman**, M.A., Isa, Y., Takemura, A., Uehara, T., 2006. Analysis of Proteinaceous
762 Components of the Organic Matrix of Endoskeletal Sclerites from the Alcyonarian *Lobophytum*
763 *crassum*. Calcified Tissue International 78, 178-185.

764 **Reitner**, J., Engeser, T.S., 1987. Skeletal structures and habitats of Recent and fossil
765 *Acanthochaetetes* (subclass Tetractinomorpha, Demospongiae, Porifera). Coral Reefs 6, 13-18.

766 **Richter**, R., 1929. Das Verhältnis von Funktion und Form bei den Deckelkorallen.
767 Senckenbergiana 11, 57-94.

768 **Romano**, S.L., Palumbi, S.R., 1996. Evolution of scleractinian corals inferred from
769 molecular systematics. Science 271, 640-642.

770 **Sandberg**, P.A., 1983. An oscillating trend in Phanerozoic non-skeletal carbonate
771 mineralogy. Nature 305, 19-22.

772 **Scrutton**, C.T., 1979. Early fossil cnidarians. The origin of major invertebrate groups.
773 Academic Press, New York, 161-209.

774 **Schmahl**, W.W., Griesshaber, E., Neuser, R., Lenze, A., Job, R., Brand, U., 2004. The
775 microstructure of the fibrous layer of terebratulide brachiopod shell calcite. European Journal of
776 Mineralogy 16, 693-697.

777 **Sorauf**, J.E., 1980. Biomineralization, structure and diagenesis of the Coelenterate skeleton.
778 Acta Palaeontologica Polonica 25, 327-348.

779 **Sorauf**, J.E., 1996. Biomineralization models and skeletal structure of Phanerozoic corals, p.
780 159-185, in: G. D. S. Jr., (Ed.), The Paleontological Society Papers, The Paleontological Society
781 Papers, Pittsburgh.

782 **Stolarski**, J., 1993. Ontogenetic development and functional morphology in the early
783 growth-stages of *Calceola sandalina* (Linnaeus, 1771). Courier Forschungsinstitut Senckenberg
784 164, 169-177.

785 **Stolarski**, J., 2003. Three-dimensional micro- and nanostructural characteristics of the
786 scleractinian coral skeleton: A biocalcification proxy. Acta Palaeontologica Polonica 48, 497-
787 530.

788 **Stolarski**, J., Mazur, M., 2005. Nanostructure of biogenic versus abiogenic calcium
789 carbonate crystals. Acta Palaeontologica Polonica 50, 847-865.

790 **Stolarski**, J., Meibom, A., Przenioslo, R., Mazur, M., 2007. A Cretaceous Scleractinian coral
791 with a calcitic skeleton. Science 318, 92-94.

792 **Stolarski**, J., Kitahara, M.V., Miller, D.J., Cairns, S.D., Mazur, M., Meibom, A., 2011. The
793 ancient evolutionary origins of Scleractinia revealed by azooxanthellate corals. BMC
794 Evolutionary biology 11, 316.

795 **Tambutté**, S., Holcomb, M., Ferrier-Pagès, C., Reynaud, S., Tambutté, É., Zoccola, D.,
796 Allemand, D., 2011. Coral biomineralization: From the gene to the environment. Journal of
797 Experimental Marine Biology and Ecology 408, 58-78.

798 **Termier**, H., Termier, G., 1948. Étude sur *Calceola sandalina* Linné. La Revue Scientifique
799 86, 208-218.

800 **Towe**, K.M., 1978. Do trilobites have a typical arthropod cuticle? Palaeontology 21, 459-
801 461.

802 **Vendrasco**, M.J., Checa, A., Heimbrock, W.P., Baumann, S.D., 2013. Nacre in molluscs
803 from the Ordovician of the midwestern United States. Geosciences 3, 1-29.

804 **Wang**, H.C., 1950. A revision of the zoantharia rugosa in the light of their minute skeletal
805 structures. Philosophical Transactions B 234, 175-246.

806 **Wang**, H.C., Chen, J.Q., 1989. Microskeletal structures and classification of rugose corals.
807 Mem. Ass. Australas. Palaeontols. 8, 179-190.

808 **Williams**, A., Wright, A.D., 1970. Shell structure of the Craniacea and other calcareous
809 inarticulate Brachiopoda. Special Papers in Palaeontology 7, 1-51.

810 **Wright**, A.J., 2010. Septal architecture and palaeoecology of *Calceola* (Cnidaria,
811 Calceolidae), with comments on the phylogeny of Devonian operculate tetracorals. Memoirs of
812 the Association of Australasian Palaeontologists 39, 159-176.

813

814 **Figure captions**

815

816 **Fig. 1.** Selected views, of macroscopic features, of *Calceola sandalina* from the Palaeontology
817 Department of Universidad Complutense de Madrid. (A) Corallite with operculum (scale bar 1
818 cm). (B) Corallite with operculum in calical view (scale bar 5 mm). (C) View of a calix showing

819 major (white arrows) and minor septa separated by desmocyte scars (white circle) and K-septum
820 (scale bar 5 mm).

821 **Fig. 2.** Structural features. (A-C) Synthetic sketch of *Calceola* with the movement of the
822 operculum and the change of gravity centre. Modify of Galle and Ficner (2004). (D) Synthetic
823 sketch of the sections analysed in this study. (E) Transversal section where can be seeing the
824 composed-septa and merged septa and the location of EBSD maps (scale bar 2 mm). (F)
825 Transverse section of a calical area, where the EBSD maps and CIP areas are shown (scale bar 1
826 mm). White arrows point to two RAD as reference of the two sections.

827 **Fig. 3.** Microscopic features of studied taxa. F: Fibres, G: Granules. (A) Transverse section
828 showing a Rapid Accretion Deposit (RAD) in the hingeline limit surrounded by lamellae (scale
829 bar 100 μm). Inset of the RAD with a granular microstructure (scale bar 200 μm). (B) Lamellar
830 sclerenchyma in the composed-septa area (scale bar 100 μm). (C) Fibres development in
831 desmocyte scar in the composed-septa area (scale bar 100 μm). Inset showing the cupolar
832 morphology of lamellae (scale bar 50 μm). (D-F) SEM images showing the microscopic
833 features of lamellae. (D) 'Scutellate' lamellae from the composed septa area (scale bar 10 μm).
834 (E) Plier-shaped lamellae from the merged septa area (scale bar 5 μm). (F) Large 'scutellate'
835 undulated lamellae from the merged septa area (scale bar 10 μm). Note the wavy structure and
836 the submicrometric structuration in the inset (scale bar 2 μm).

837 **Fig. 4.** AFM images of the nanostructure in *Calceola*. (A-B) Height and phase images in the
838 contact of two lamellae (black dashed line, scale bar 500 nm). Note the arrows point to the c-
839 axis orientation of microcrystals. (C-D) Height and phase images of the nanotexture of a
840 microcrystal with plier-shaped (scale bar 1.25 μm). Note the intralamination that form the
841 microcrystal and the misorientation between crystals (black dashed line). (E-G) Height, phase
842 and amplitude images of a contact area (black dashed line) between two microcrystals co-
843 oriented (scale bar 270 nm). (H) Phase image where the pill-shaped nanotexture can be
844 observed in a transverse section of a microcrystal (scale bar 66 nm). Note the dark envelopes

845 around nanocrystals (white arrow). (I-J) Height, phase images of a longitudinal section of a
846 microcrystal showing the stacking of nanogranules forming a microcrystal (scale bar 400 nm).
847 (K-L) Height and phase image of nanotexture of a longitudinal section of a microcrystal,
848 showing the intralaminated structure of microcrystals (scale bar 180 nm).

849 **Fig. 5.** CIP analysis of a transverse section of *Calceola sandalina*. (A) Petrographic micrograph
850 of the insertion area of septa and the hingeline, showing the undulated RAD (scale bar 100 μm).
851 (B) Orientation image of the studied area (scale bar 100 μm). Inset showing the pole figure of
852 the entire investigated area. (C) Petrographic micrograph of the insertion area a composed septa,
853 showing the wavy microstructure (yellow arrows points to the septal ridges, scale bar 100 μm).
854 (D) Orientation image of the studied area (scale bar 100 μm). Inset showing the pole figure of
855 the entire investigated area. (E) Petrographic micrograph of the hemispheric RAD surrounded
856 by a lamellar sclerenchyma (scale bar 50 μm). (F) Orientation image of the studied area (scale
857 bar 50 μm). Inset showing the pole figure of the entire investigated area. Pole figures were
858 calculated as an orientation distribution function and provided in multiples of uniform
859 distribution intervals of 0.5 for *c*-axis orientations. Red points correspond to the punctual *c*-axis
860 orientation of each pixel of selected areas, I (RAD), II (upward lamellae) and III (RAD). Last
861 circle correspond with the standard colour look-up table (CLUT).

862 **Fig. 6.** Crystallography of composed-septa area (A-B), scale bar 60 μm ; desmocyte scar (C-D),
863 scale bar 35 μm and a detail of dendritic-like structure of septal area (E-F), scale bar 15 μm . (A,
864 C, E) Index intensity maps, showing the microstructural features of studied area. (B, D, F)
865 Crystallographic orientation maps, showing the main crystallographic orientations in the studied
866 areas. Note the gradual transition between the lamellae and the fibres of desmocyte scar in (D)
867 and the co-orientation in the plier-shaped lamellae in (F). Pole figures and ODF pole figures (in
868 normal direction view (ND) to the sample surface in a three axes reference system with
869 indication of the reference (RD) and transverse (TD) directions) indicating crystallographic
870 orientation of calcite crystals in reference to the *c* axes; and crystallographic key indicating

871 colour coding of crystallographic axes. I-III correspond with the (A-B) maps, and IV-VI
872 corresponds with (C-D) maps.

873 **Fig. 7.** Crystallography of and hemispheric Rapid Accretion Deposits (RAD). (A) Index
874 intensity maps, showing the microgranular arrangement of the deposit (scale bar 25 μm). Note
875 the thick none-diffraction areas around microcrystals and the rise of crystallinity toward outside
876 the RAD. (B) Crystallographic orientation maps, showing the main crystallographic orientations
877 of the studied area (scale bar 25 μm). Note the gradual organisation of the crystals toward
878 outside the RAD. Pole figures (in normal direction view (ND) to the sample surface in a three
879 axes reference system with indication of the reference (RD) and transverse (TD) directions)
880 indicating crystallographic orientation of calcite crystals in reference to the c axes; and
881 crystallographic key indicating colour coding of crystallographic axes.

882 **Fig 8.** EMPA mapping of a transversal section of *Calceola* (scale bar 50 μm). (A) BSE image of
883 the Rapid Accretion Deposits (RAD). Note the difference in colour between the RAD and the
884 lamellar sclerenchyma. (B-F) Mapping of different elements (Ca, Mg, Sr, S).

885 **Fig. 9.** (A) Graph showing the distribution of the amounts the Ca, Mg, Sr, S along of a Rapid
886 Accretion Deposit (RAD). (B) BSE image locating the analysed points (yellow dots, scale bar
887 100 μm). (C) Linear regressions of mol % MgCO_3 versus CaCO_3 and table showing the
888 parameters of linear regression.

889 **Fig. A1.** Crystallography of merged septa area (A-B), scale bar 45 μm and K-septum (C-D),
890 scale bar 50 μm . (A-C) Index intensity maps, showing the microstructural features of studied
891 area. (B-D) Crystallographic orientation maps, showing the main crystallographic orientations
892 in the studied area. Note the variation in orientation between the major septa in green coloration
893 and minor septum in purple coloration in (B). Pole figures and ODF pole figures (in normal
894 direction view (ND) to the sample surface in a three axes reference system with indication of the
895 reference (RD) and transverse (TD) directions) indicating crystallographic orientation of calcite
896 crystals in reference to the c axes; and crystallographic key indicating colour coding of

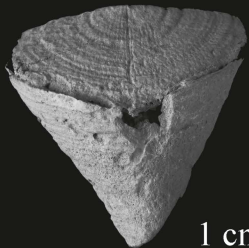
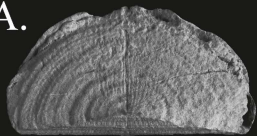
897 crystallographic axes. I-III correspond with the (A-B) maps, and IV-VI corresponds with (C-D)
898 maps.

899 **Fig. A2.** Relative frequency (%) of the misorientation angles of different taxa studied
900 by EBSD.

901

Operculum

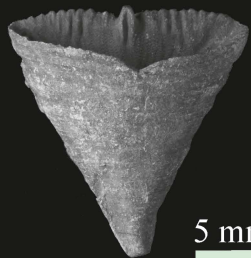
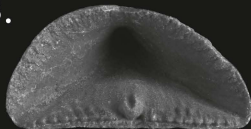
A.



1 cm

Calix

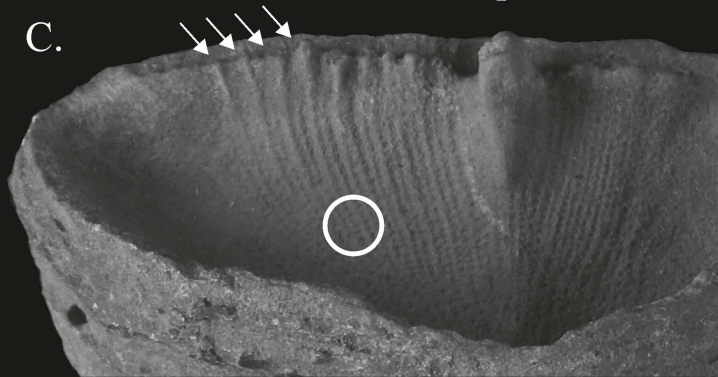
B.



5 mm

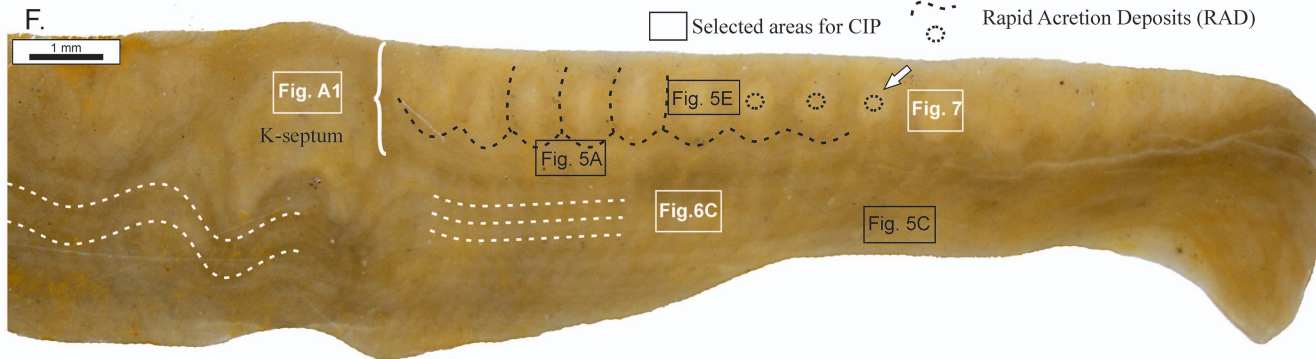
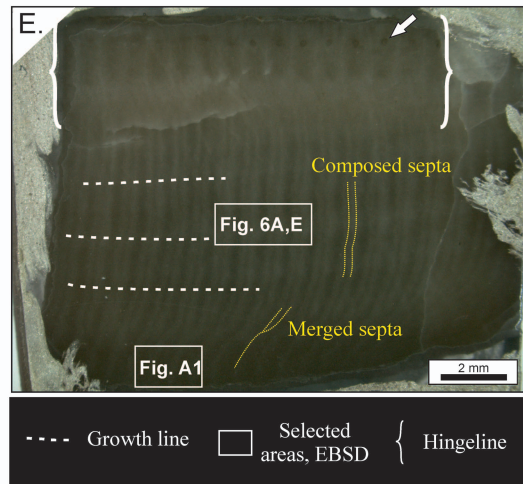
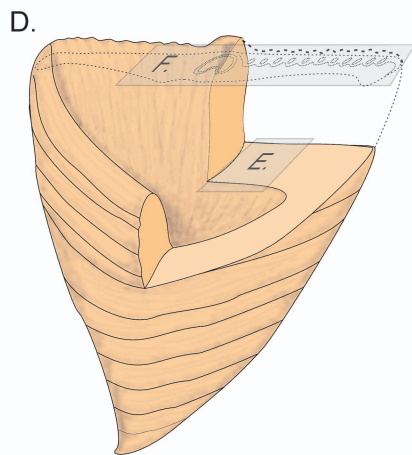
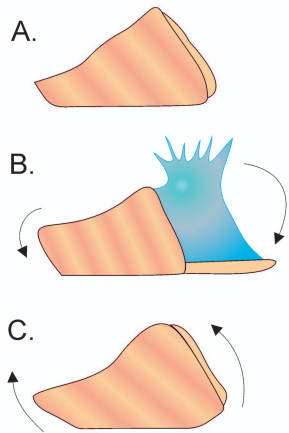
K-septum

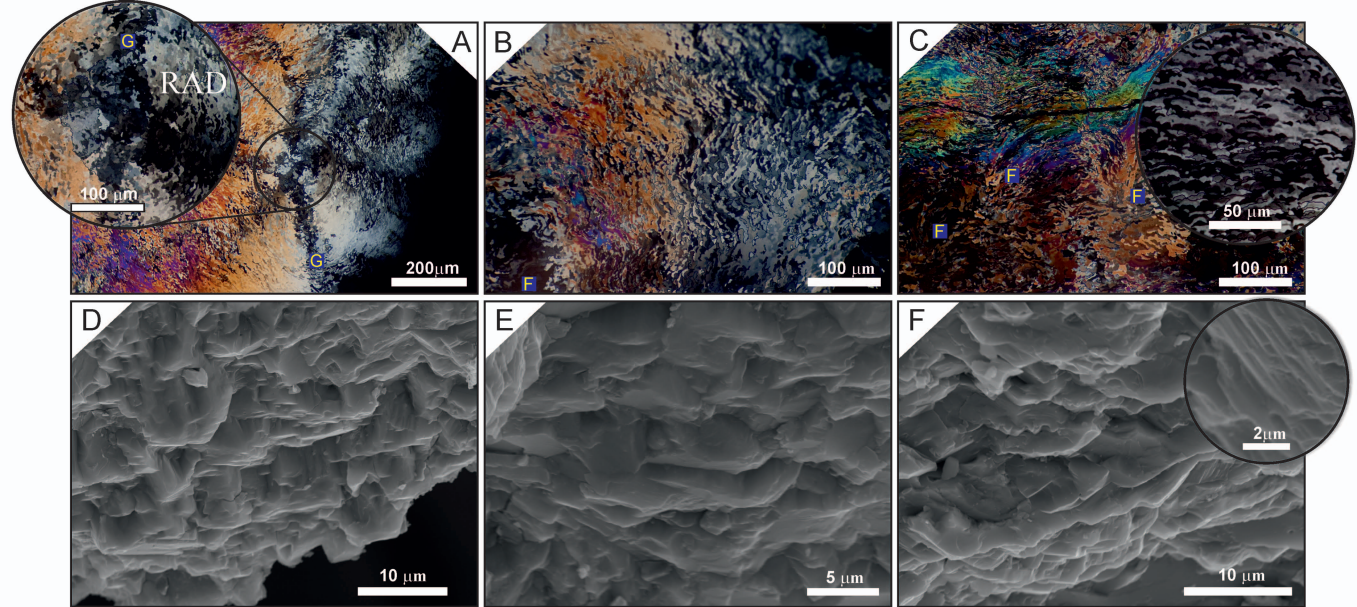
C.

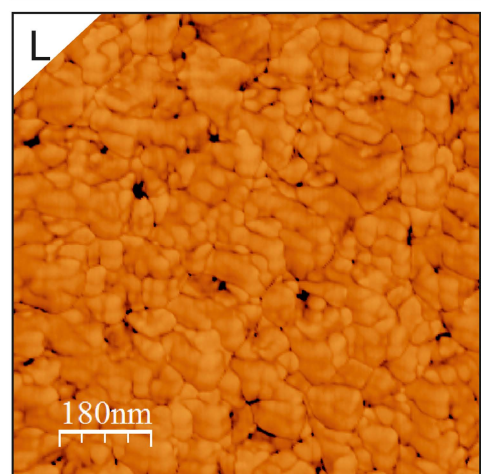
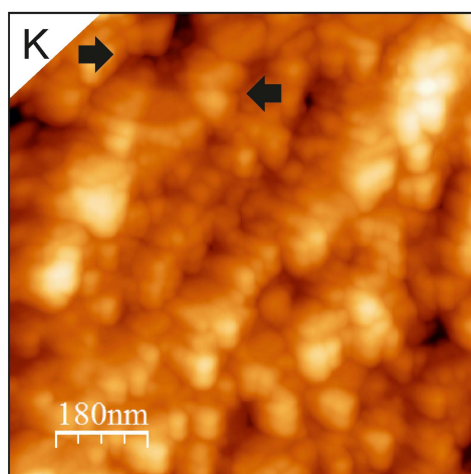
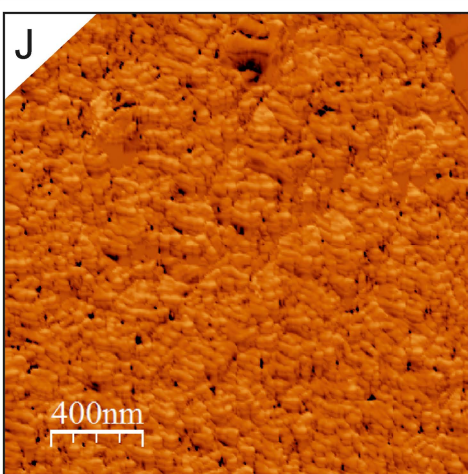
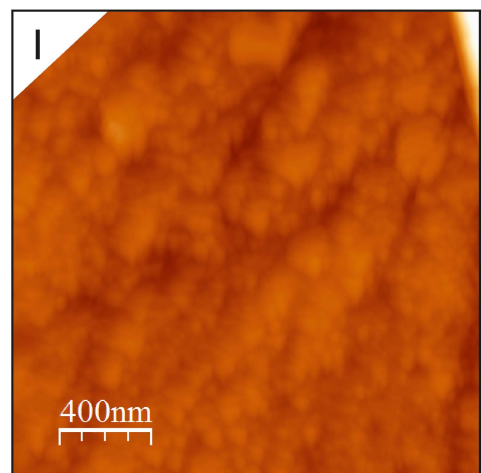
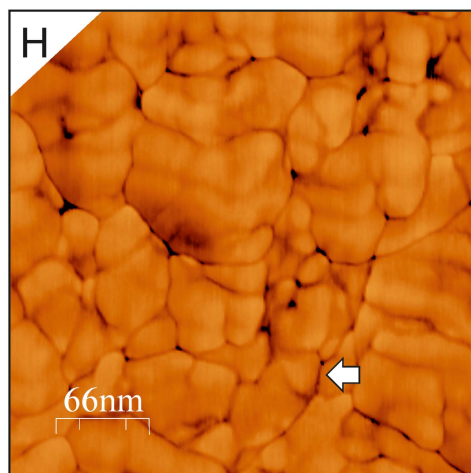
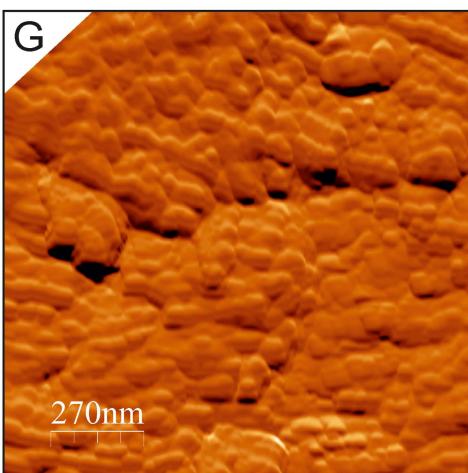
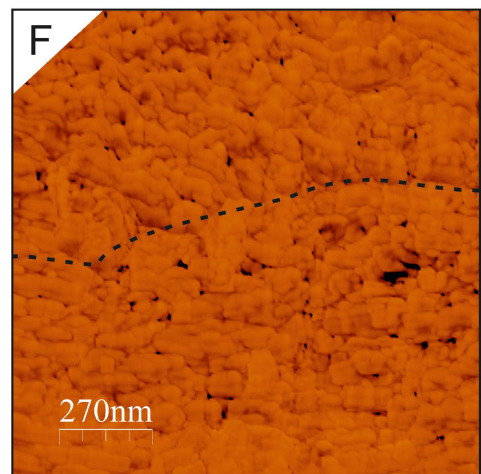
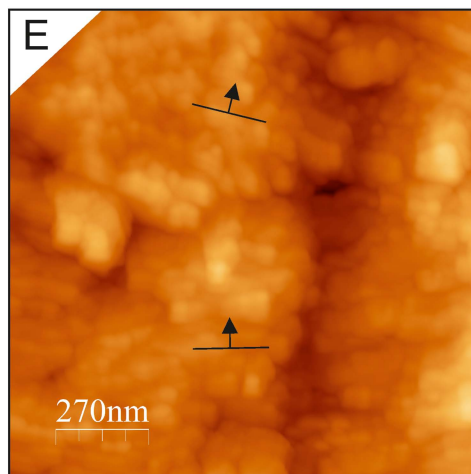
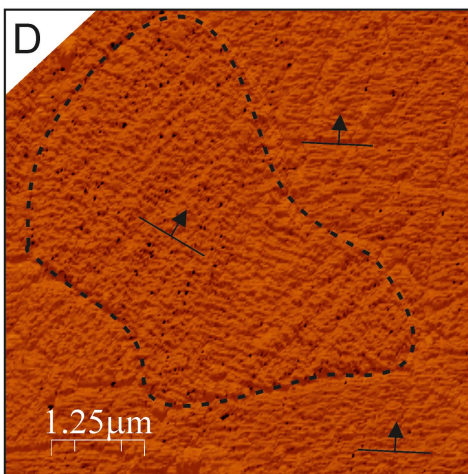
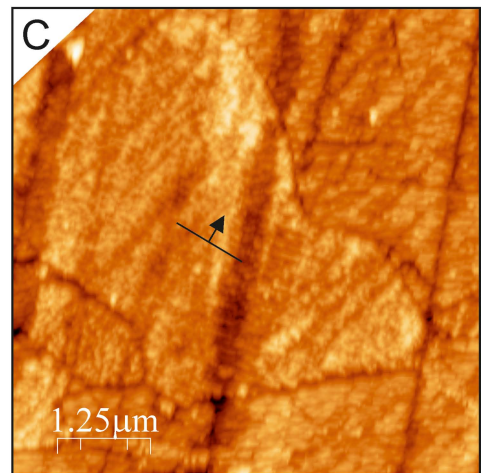
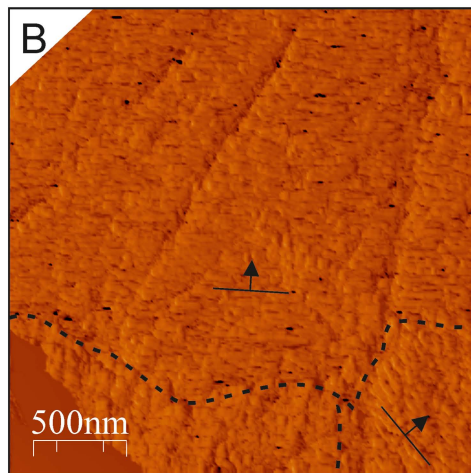
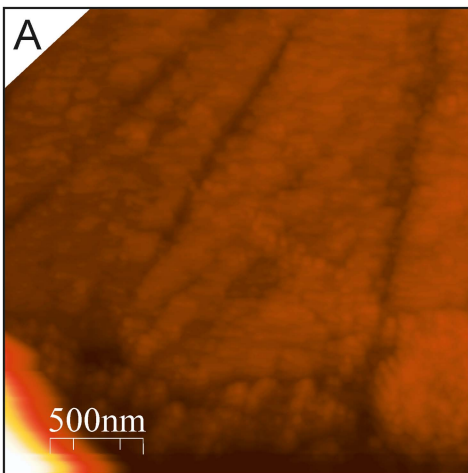


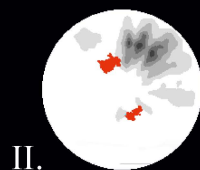
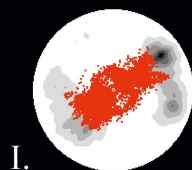
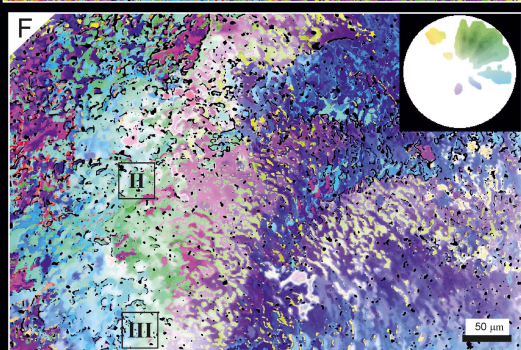
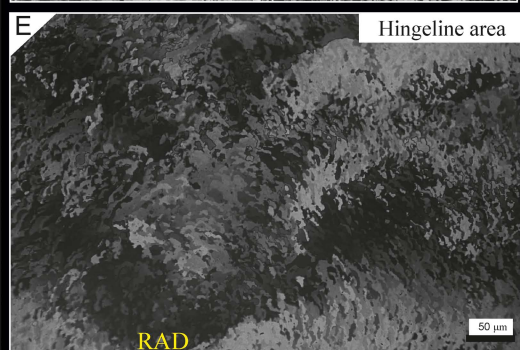
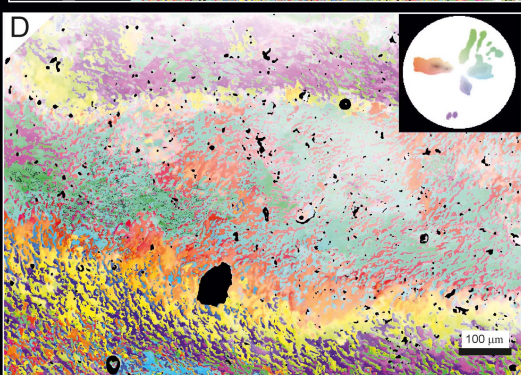
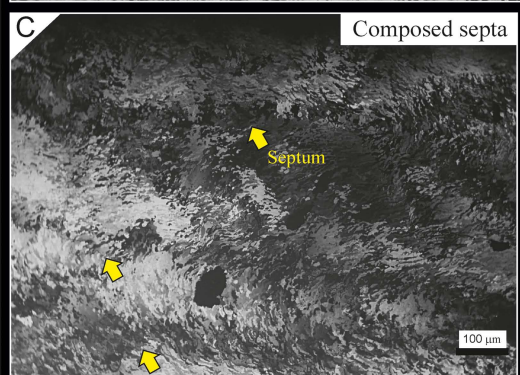
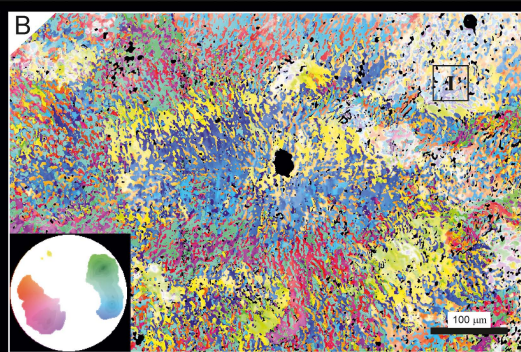
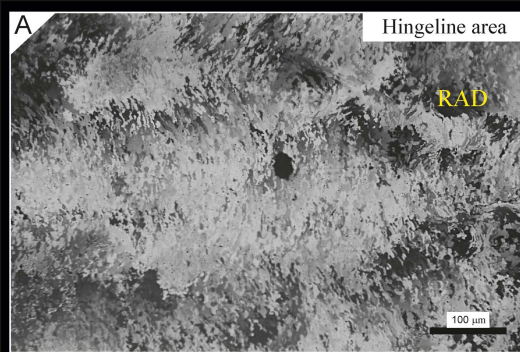
○ Desmocyte scars

5 mm

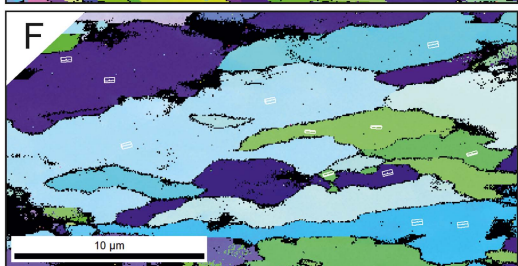
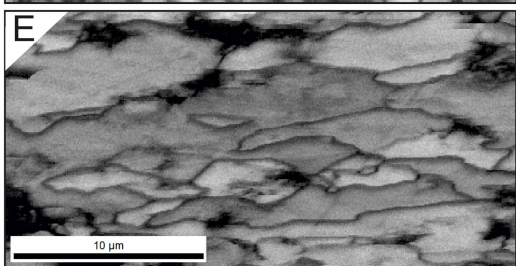
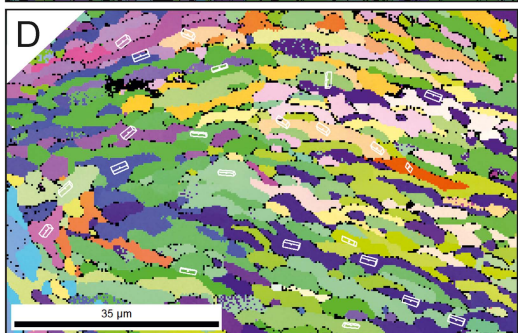
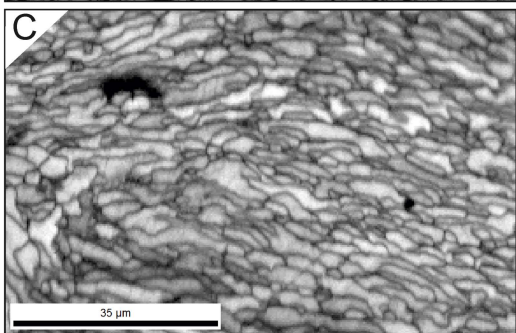
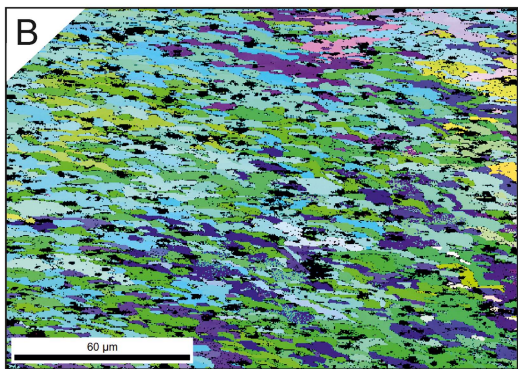
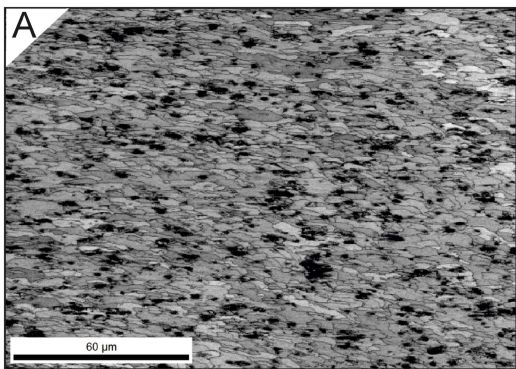




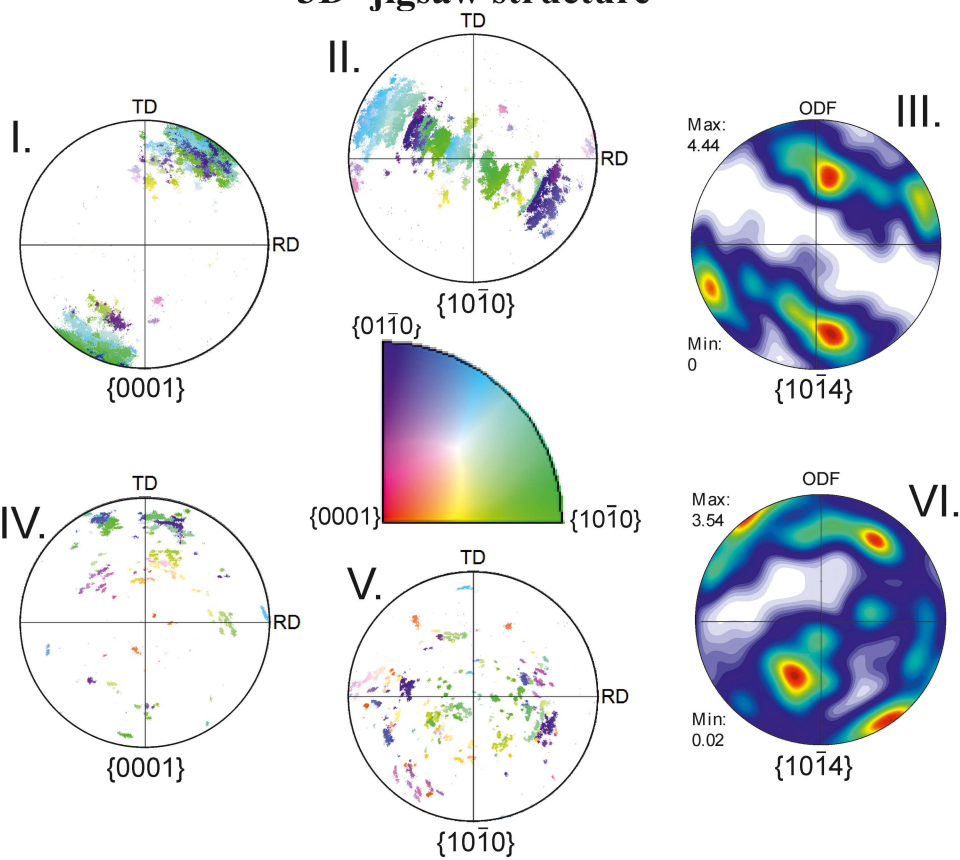


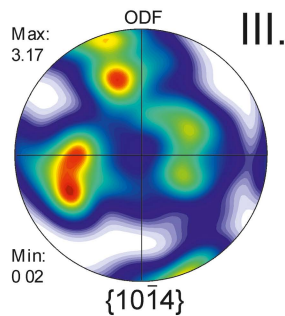
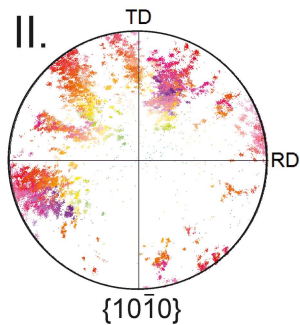
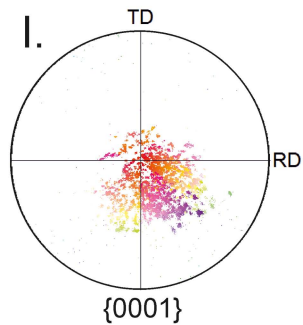
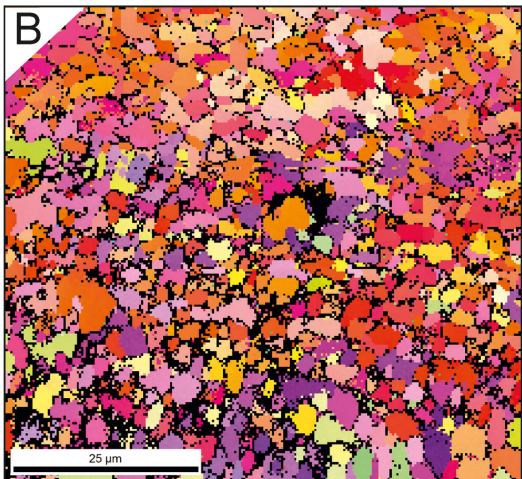
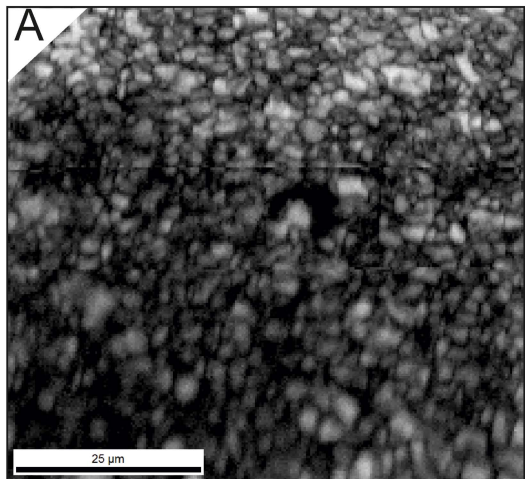


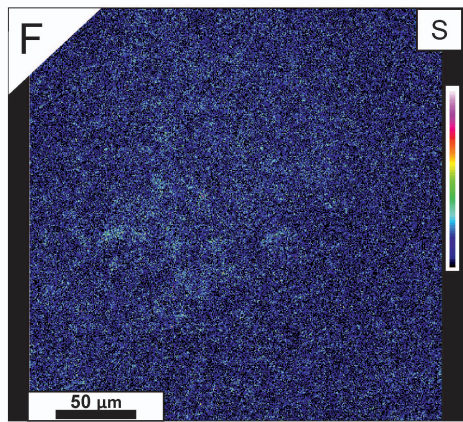
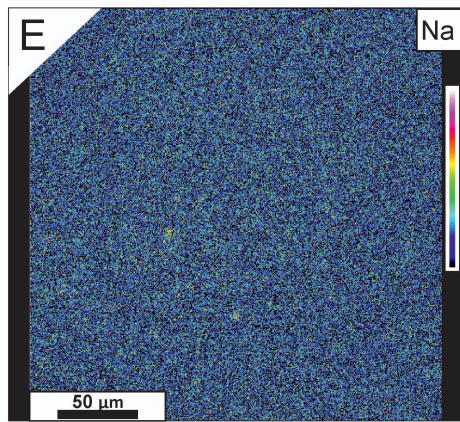
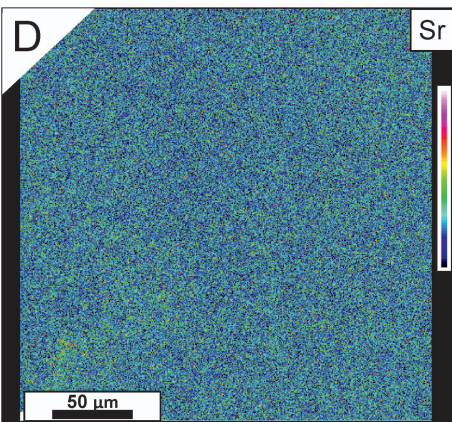
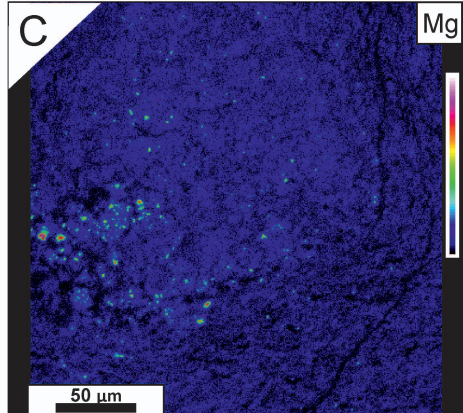
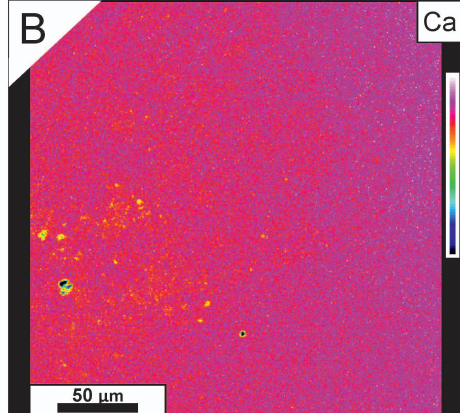
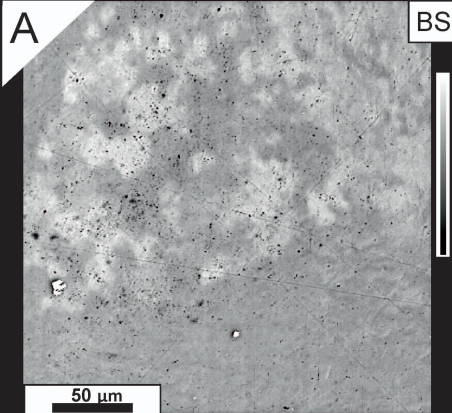
Colour coding

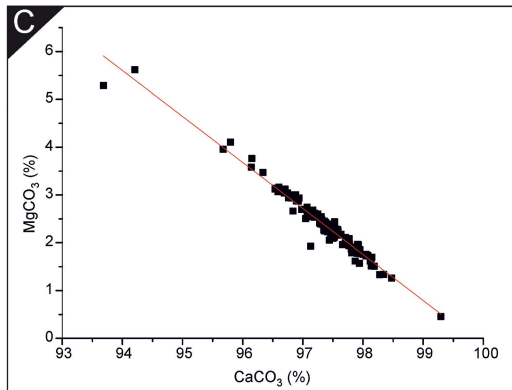
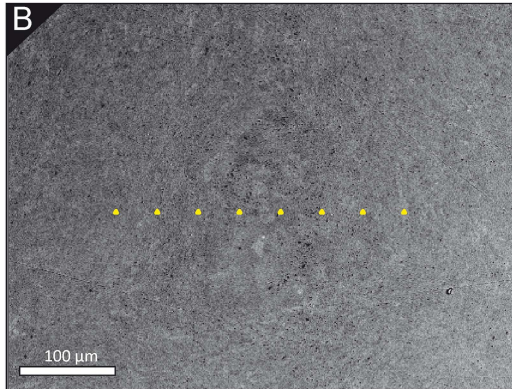
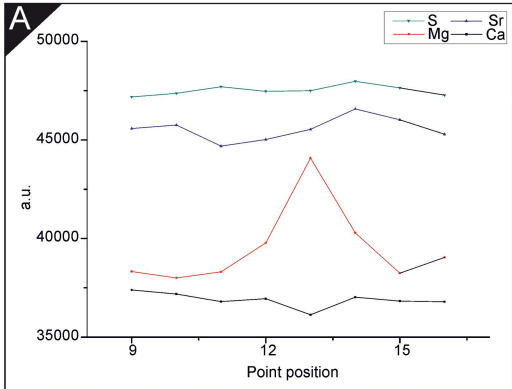


3D- jigsaw structure









Equation	$y = a + b \cdot x$		
Adj. R-Square	0.96541		
		Value	Standard Error
MgCO_3	Intercept	96.08643	1.65363
MgCO_3	Slope	-0.96256	0.01699

